iScience

Article

Adenosine deficiency facilitates CA1 synaptic hyperexcitability in the presymptomatic phase of a knockin mouse model of Alzheimer disease

Graphical abstract

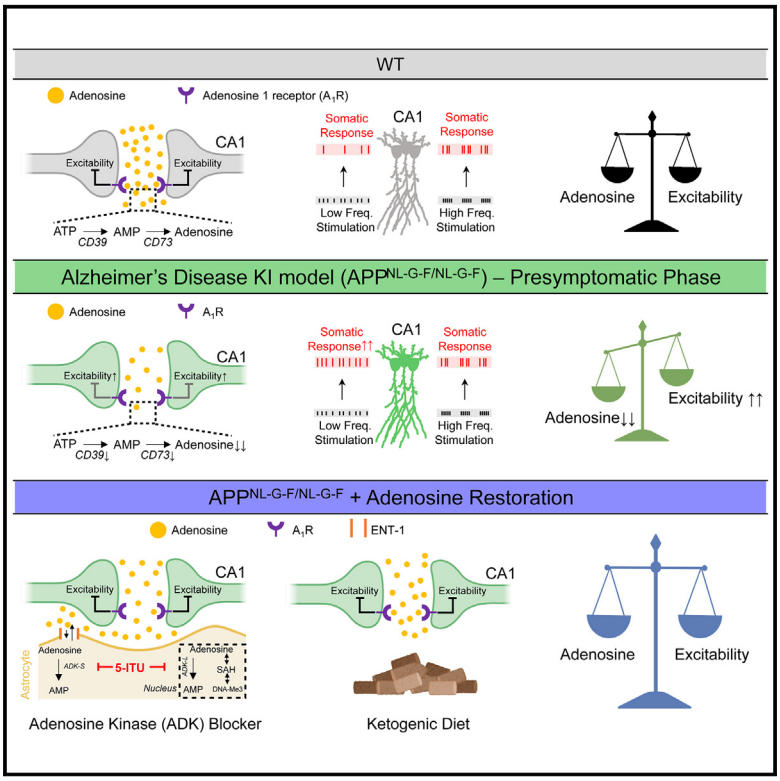

Highlights

- Synaptic hyperexcitability spreads to the soma at low frequencies of stimulation
- Reduced adenosine tone facilitates synaptic hyperexcitability *in vitro* and *in vivo*
- ATP-to-adenosine extracellular conversion drives reduced adenosine tone
- Restoring adenosine tone normalizes neuronal excitability in the AD model

Authors

Mattia Bonzanni, Alice Braga, Takashi Saito, Takaomi C. Saido, Giuseppina Tesco, Philip G. Haydon

Correspondence

mab4092@med.cornell.edu (M.B.), philip.haydon@tufts.edu (P.G.H.)

In brief

Biological sciences; Neuroscience; Molecular neuroscience

Bonzanni et al., 2025, iScience *28*, 111616
January 17, 2025
https://doi.org/10.1016/j.isci.2024.111616

CellPress

iScience

CellPress
OPEN ACCESS

Article

Adenosine deficiency facilitates CA1 synaptic hyperexcitability in the presymptomatic phase of a knockin mouse model of Alzheimer disease

Mattia Bonzanni,[1,4,6,*] Alice Braga,[1,5,6] Takashi Saito,[2] Takaomi C. Saido,[3] Giuseppina Tesco,[1] and Philip G. Haydon[1,7,*]
[1]Department of Neuroscience, Tufts University, Boston, MA 02111, USA
[2]Department of Neurocognitive Science, Institute of Brain Science, Nagoya City University Graduate School of Medical Sciences, Nagoya, Aichi 467-8601, Japan
[3]Laboratory for Proteolytic Neuroscience, RIKEN Center for Brain Science, 2-1 Hirosawa, Wako, Saitama 351-0198, Japan
[4]Present address: Department of Pediatrics, Weill Cornell Medicine, New York City, NY, 10065, USA
[5]Present address: Center for Cardiovascular and 811 Metabolic Neuroscience, Department of Neuroscience, Physiology & Pharmacology, University 812 College London, London, WC1E 6BT, UK
[6]These authors contributed equally
[7]Lead contact
*Correspondence: mab4092@med.cornell.edu (M.B.), philip.haydon@tufts.edu (P.G.H.)
https://doi.org/10.1016/j.isci.2024.111616

SUMMARY

The disease's trajectory of Alzheimer disease (AD) is associated with and negatively correlated to hippocampal hyperexcitability. Here, we show that during the asymptomatic stage in a knockin (KI) mouse model of Alzheimer disease ($APP^{NL-G-F/NL-G-F}$; APPKI), hippocampal hyperactivity occurs at the synaptic compartment, propagates to the soma, and is manifesting at low frequencies of stimulation. We show that this aberrant excitability is associated with a deficient adenosine tone, an inhibitory neuromodulator, driven by reduced levels of CD39/73 enzymes, responsible for the extracellular ATP-to-adenosine conversion. Both pharmacologic (adenosine kinase inhibitor) and non-pharmacologic (ketogenic diet) restorations of the adenosine tone successfully normalize hippocampal neuronal activity. Our results demonstrated that neuronal hyperexcitability during the asymptomatic stage of a KI model of Alzheimer disease originated at the synaptic compartment and is associated with adenosine deficient tone. These results extend our comprehension of the hippocampal vulnerability associated with the asymptomatic stage of Alzheimer disease.

INTRODUCTION

Alzheimer disease (AD) is a progressive neurodegenerative condition marked by the abnormal buildup of amyloid beta (Aβ) plaques, the formation of neurofibrillary tau tangles, and progressive neural degeneration.[1] Along with the hallmarks of the disease, neuronal hyperactivity has been reported in patients, animal models, and in patient-derived cell cultures.[2–12] Previous studies[13] have found that both sporadic and familial AD patients exhibit increased cortical-hippocampal activity, occurrence of seizures during the early phases of the prodromal stage,[14–16] and faster cognitive decline in patients who exhibit subclinical epileptiform activity.[17–19] Moreover, new evidence has linked Aβ-driven hyperactivity to subsequent aggregation and spreading of tau pathology,[20] whereas phosphorylated tau has been associated with hypoactive hippocampal activity.[21] Despite the evident comorbidity between neuronal hyperactivity and AD during the prodromic stage in patients, the origin of neuronal hyperexcitability and hippocampal vulnerability remain debated.[22,23] It is noteworthy that some reports have described hippocampal hyperactivity in asymptomatic offspring of autopsy-confirmed AD patients.[24,25] Granted that such evidence is limited, it raises the hypothesis that hippocampal hyperexcitability may precede the prodromal stage also in humans. In fact, early-stage murine models of AD exhibit hippocampal hyperactivity,[4,13,26,27] which contributes to the deposition of amyloid beta and is promoted by amyloid beta toxicity,[28] calcium imbalance,[29] enhanced glutamate signaling,[30] and decreased GABA tone. Since it has been shown[31] that breaking the vicious cycle between amyloid beta deposition and neuronal hyperexcitability ameliorated the disease's trajectory, it is of relevance to unravel the players contributing to this aberrant activity at early stage of the disease. Since multiple mechanisms converge to control neuronal hyperactivity, additional contributors remain unexplored. Further investigation is needed to examine understudied factors contributing to the neuronal hyperexcitability during the asymptomatic (preclinical) phase of AD,[1] with the goal of understanding the origin of the functional hippocampal vulnerability during the earliest stages of AD. Our objective was to investigate novel drivers of electrophysiological compensatory mechanisms that develop during the preclinical phase,[32] as these insights will clarify the disease trajectory and might

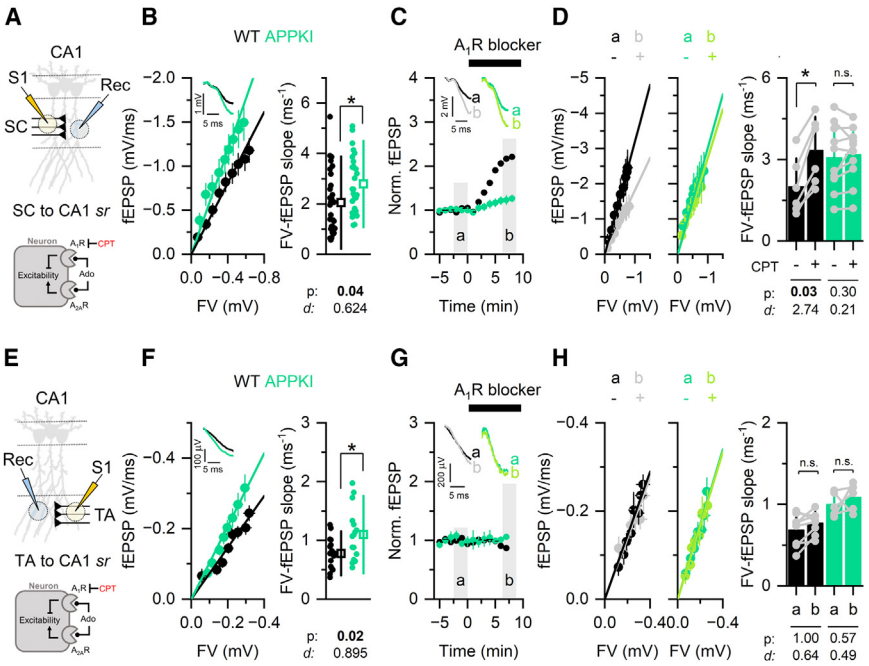

Figure 1. SC and TA synaptic signaling in the APPKI model is enhanced in an adenosine-dependent and independent manner, respectively

(A and E) Top: scheme of experiment to monitor SC-to-CA1 and TA-to CA1 synaptic signaling (S1: stimulation; Rec: recording). Bottom: cartoon of adenosine signaling.

(B and F) Mean fEPSP-FV relationship (left) and individual slope data points (right); SC-to-CA1; WT: $n = 30/16$, APPKI: $n = 27/17$; TA-to-CA1—WT: $n = 18/11$, APPKI: $n = 16/9$. Inset: representative fEPSP traces.

(C and G) Time trajectory of normalized fEPSP before (a) and after (b) the dosage of the A_1R blocker, CPT (200 nM).

(D and H) Mean fEPSP-F.V. relationship (left) and individual paired slope data points (right) before (a) and after (b) dosage of the A_1R blocker; SC-to-CA1; WT: $n = 12/3$, APPKI: $n = 20/6$; TA-to-CA1—WT: $n = 16/4$, APPKI: $n = 10/5$. p: p value; d: Cohen's effect size. Mean ± S.D. n = n. slices/n. mice. Statistic: generalized linear mixed effect models. Black: WT, green: APPKI, gray: WT + CPT, light green: APPKI+CPT.

potentially lead to novel therapeutic interventions aimed at reversing these adverse effects.[1]

Adenosine is a neuromodulator regulating both inhibitory and excitatory neuronal responses primarily through A_1 and A_{2A} receptors.[33] Furthermore, adenosine influences the state of DNA methylation.[34] Although dysregulated adenosine signaling, mainly acting through the $A_{2A}R$ axis, has been observed during the symptomatic stages of AD,[35] it is unclear whether adenosine signaling is affected during the asymptomatic stage of AD. Attempts to slow the progression of the disease by either chronically depressing[36] or potentiating[37,38] the adenosine signaling have produced contradictory results, highlighting the complexity of the issue. Adenosine functions as a "retaliatory metabolite," serving as a feedback control mechanism in response to low-energy states that may occur during aberrant neuronal activity. Given its anticonvulsant and antiepileptogenic properties,[33] along with our limited comprehension of the connection between adenosine signaling, hyperexcitability, and AD, we asked whether reduced adenosine signaling might participate in the hyperexcitable phenotype during the preclinical phase of AD.

In this work, we present evidence of a link between adenosine deficiency and hippocampal synaptic hyperactivity during the asymptomatic phase in a KI model of AD.

RESULTS

CA1 synaptic activity is potentiated in the asymptomatic phase of the APPKI model

Synaptic alterations have been described as one of the earliest events in AD.[26] Considering the vulnerability of the entorhinal cortex-hippocampus (EC-Hip) circuitry in both human and murine AD models,[39] we monitored the CA1 field, which serves as the converging site for two distinct pathways within the EC-Hip axis: the indirect pathway from CA3 to CA1 (Schaffer collateral [SC]) and the direct pathway from ECIII to CA1 (temporoammonic [TA] pathway). We tested the hypothesis that net synaptic transmission is potentiated in these two circuits in the APPKI model.

We monitored the CA1 *sr* (*stratum radiatum*) response by stimulating either the SC (Figures 1A–1D) or TA terminals (Figures 1E–1H) in the hippocampal slices from wild-type [WT] (black) and APPKI (green) mice at 8 weeks of age, an asymptomatic stage of the diseases with minimal to no plaque burden and absent tau pathology, gliosis, spine and cellular degeneration, and cognitive impairment.[26] This time point corresponds to the decade-long asymptomatic phase in AD patients, where the disease gradually progresses from reversible, compensatory cellular mechanisms in response to proteopathic stress to the irreversible clinical manifestations.[32] We measured the evoked fEPSP (field excitatory postsynaptic potential) and FV (fiber volley) responses as a proxy of postsynaptic activity and presynaptic recruitment, respectively. We then quantified net synaptic transmission of each slice as the slope of the FV-fEPSP relationship (Figures 1B and 1F), where larger absolute values indicate an increased net synaptic transmission. As evident from the representative traces (insets) and the FV-fEPSP slope distributions, net synaptic transmission was potentiated in the APPKI model in both circuits (Figures 1B and 1F, respectively); the FV response was not different between the genotypes, indicating that the same fraction of pre-synaptic fibers has been activated during stimulation (Figure S1). It follows that, given the same pre-synaptic activation (FV), the post-synaptic response (fEPSP) is potentiated in the APPKI model (Figures 1B and 1F, left).

These results demonstrated an increased net synaptic activity in both circuits in the absence of pre-synaptic fibers degeneration during the asymptomatic stage of AD.

Enhanced synaptic transmission of SC synapses, but not TA synapses, is facilitated by adenosine deficiency in the APPKI model

Although various factors have been associated with neuronal hyperexcitability at different stages of AD,[13] the involvement of adenosine, a known endogenous anticonvulsant and antiepileptogenic neuromodulator, remains unexplored during the asymptomatic phase. We investigated whether reduced adenosine tone, known for its inhibitory role on neurons through the adenosine 1 receptor (A_1R),[33] contributed to the enhanced synaptic transmission observed in the CA1 region of the APPKI model.

To assess the A_1R-dependent basal tone, we monitored the FV-fEPSP relationship before and after delivery of an A_1R antagonist, CPT (8-cyclopentyl-1,3-dimethylxanthine, 200 nM). After computing the baseline FV-fEPSP relationship, we selected a stimulation intensity producing fEPSP with a slope that was 30%–40% of the maximal and monitored the fEPSP before (1) and after (2) dosing the A_1R blocker to confirm the steady-state action of the drug (Figures 1C and 1G). We then constructed the FV-fEPSP relationships in the presence of the blocker. In the SC to CA1 circuit, as evident from the time trajectory (Figure 1C) and further confirmed by the FV-fEPSP slope values (Figure 1D), net synaptic transmission was enhanced by the A_1R antagonist in WT but not in APPKI. In the same circuit, we also confirmed that A_1R receptors were functionally active by dosing an A_1R agonist (Figures S2A–S2D) and found a similar decrease in net synaptic transmission in both models. Additionally, pharmacological inhibition of the ENT1 transporter (Figures S2E–S2H), which, along with the ENT2 isoform, is responsible for astrocytic adenosine uptake, led to elevated extracellular adenosine concentrations, as previously[37,40] demonstrated. This increase resulted in an A_1R-mediated reduction in net synaptic transmission in both models. This finding confirmed that the APPKI model retained the A_1R-mediated inhibitory effects. Importantly, in the TA to CA1 circuit, both WT and APPKI were insensitive to the A_1R antagonist (Figures 1G and 1H), suggesting that the TA to CA1 circuit was not under basal adenosine control.

These results revealed that a potential decrease in the baseline adenosine level, with intact A_1R signaling, contributed to increased synaptic hyperexcitability at the SC terminals. Moreover, the lack of basal adenosine in the TA pathway emphasized the involvement of adenosine-independent factors in setting synaptic hyperactivity in the APP KI model.

Heterosynaptic, but not homosynaptic, plasticity is reduced in the APPKI model

Considering the adenosine-mediated modification of synaptic activity at the SC synapses in the APPKI model, we investigated whether such alterations affected synaptic plasticity. We applied homosynaptic and heterosynaptic stimulation protocols to investigate the plasticity at the SC terminals.

We monitored the fEPSP time trajectory (Figure 2B) before (Figure 2B, a) and after (Figure 2B, b) high-frequency stimulation at the SC terminals (LTP protocol, Figure 2A). The resulting synaptic potentiation was intact in both genotypes (Figure 2C). We then monitored the PPr (Paired Pulse ratio; Figure 2E), finding a similar trend for the WT and APPKI models (Figure 2F). These results demonstrated that both long- and short-term cellular memory at the SC terminals were intact in the APPKI model.

Heterosynaptic depression at the SC terminals has been previously demonstrated to require an intact adenosine tone.[40,41] Therefore, we examined the hypothesis that the APPKI model lacked heterosynaptic depression as a result of the deficient adenosine tone. We stimulated two independent SC fibers (Figures 2G, S1, and S2); the S2 electrode served as site of a single high-frequency burst (100 Hz, 1 s), resulting in transient potentiation of the synaptic transmission, whereas S1 served as site of heterosynaptic depression. To confirm pathway independence, we monitored the fEPSP amplitude at the S1 electrode either preceded or not by a 50-ms stimulation of the S2 electrode (Figure 2H). Our results (Figure 2I) indicated that the normalized fEPSP amplitude after S1 stimulation showed no significant difference, regardless of whether the S2 stimulation was performed or not, thus confirming pathway independence. In response to a 1s 100 Hz stimulation at the S2 site (Figure 2J), synaptic activity at this site was similarly potentiated in both genotypes. At the S1 site, synaptic depression was present in both genotypes, though significantly more prominent in the WT vs. APPKI (Figure 2K) model.

These results demonstrated that homosynaptic plasticity remains unaffected, whereas heterosynaptic depression was reduced in the APP KI model. The evidence of a reduced heterosynaptic depression further supported the idea of a decreased adenosine tone since intact adenosine signaling is required for this form of plasticity.

Enhanced CA1 somatic activity mirrors the synaptic potentiation in the APPKI model

Although WT and APPKI mice exhibited distinct synaptic responses, we asked whether somatic excitability was similarly enhanced. We first recorded the population spike (PS) at CA1 *pyr* (*stratum pyramidale*) in response to SC stimulation (Figures 3A and 3B). Net somatic activity was determined by monitoring the FV-PS amplitude relationship (Figure 3C). APPKI had increased net somatic activity (Figure 3C). The A_1R antagonist CPT augmented PS in both genotypes although to different magnitudes (Figures 3D and 3E; see effect sizes). To ask whether the increased PS was a direct reflection of synaptic potentiation, we also monitored the fEPSP-FV relationship (Figure 3F). When normalized by synaptic activity, the somatic output was not different between the two genotypes (Figure 3F). These results demonstrated that the enhanced synaptic activity at SC synapses is transmitted to the somatic compartment and that there is no further facilitation at the soma. These results suggested that the A_1R-dependent hyperexcitable phenotype primarily occurs at the synaptic level.

To examine the somatic response in the TA pathway, we utilized a stimulus protocol that more faithfully resembles those found *in vivo* (naturalistic stimulation; Figures 3I and 3J), as sparse stimulation fails to elicit population spikes.[42] In Figure 3K, we report the probability of generating a population spike (PS Prob.) as a function of the frequency of stimulation. We first confirmed that the capability to generate population spikes during a naturalistic stimulation protocol was similar across conditions (WT, WT + CPT, APPKI, APPKI+CPT; Figure 3K). Although

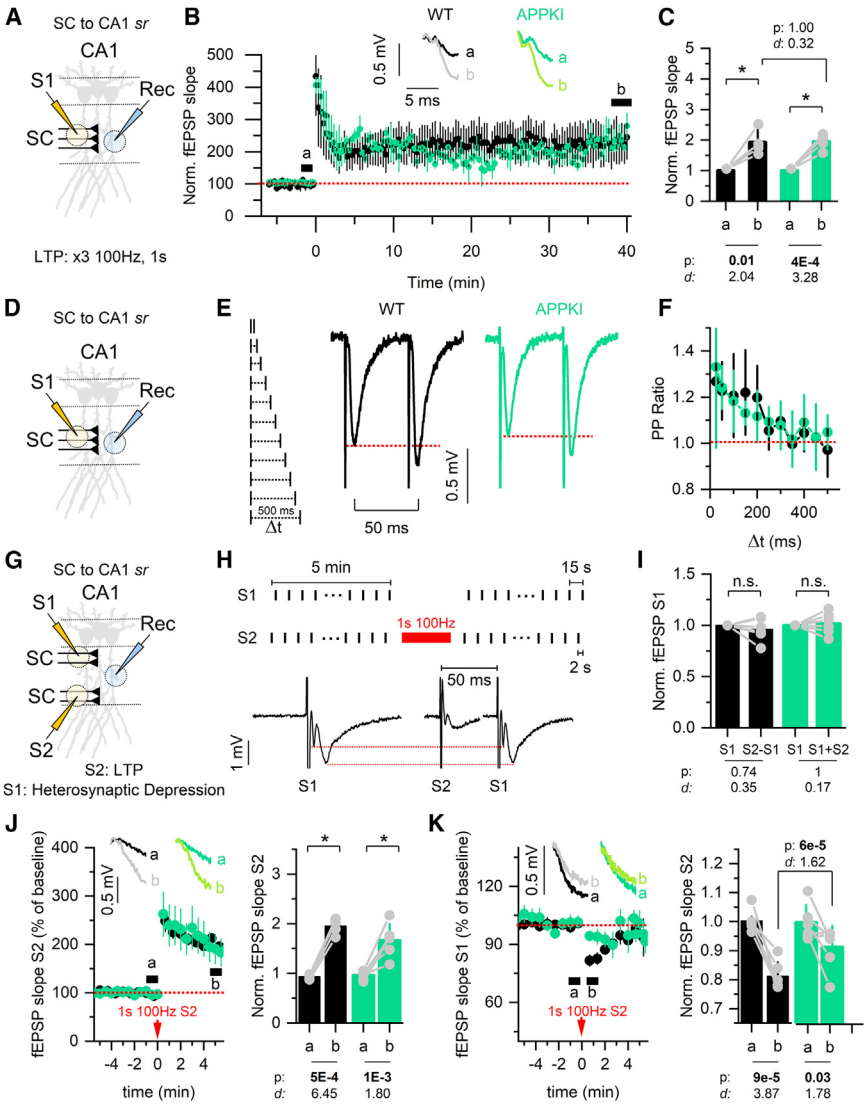

Figure 2. Heterosynaptic, but not homosynaptic, plasticity is affected at the SC terminals of the APPKI model

(A, D, and G) Scheme of experiment to monitor SC-to-CA1 and TA-to CA1 synaptic signaling (S1: stimulation fiber tract 1; S2: stimulation fiber tract 2; Rec: recording).

(B) Mean normalized fEPSP time trajectory before and after LTP protocol (at time = 0 min; x3 100Hz stimulation, 1 s duration, 15 s inter-stimulus interval). Inset: representative fEPSP traces.

(C) Mean normalized fEPSP before (a) and after (b) LTP protocol and individual data points; WT: n = 4/4, APPKI: n = 4/4.

(E) Paired pulse (PP) protocol with incremental inter-stimulation interval (Δt) (left) and representative traces at Δt = 50 ms (right).

(F) Mean PP Ratio as a function of Δt; WT: n = 6/4, APPKI: n = 7/6.

(H) Heterosynaptic depression stimulation protocol (top) and representative traces (bottom) showing the independence of the two pathways S1 and S2; fEPSP elicited at S1 does not change when is preceded by S2 stimulation.

(I) Mean fEPSP of S1 alone and S2+S1 (Δt = 50 ms) normalized on S1 alone; WT: n = 6/6, APPKI: n = 6/6.

(J) Left: mean normalized S2 fEPSP time trajectory before (a) and after (b) S2 1s 100 Hz stimulation. Inset: representative fEPSP traces. Right: mean normalized S2 fEPSP before (a) and after (b) S2 stimulation and individual data points; WT: n = 5/5, APPKI: n = 6/6.

(K) Left: mean normalized S1 fEPSP time trajectory before (a) and after (b) S2 1s 100 Hz stimulation. Inset: representative fEPSP traces. Right: mean normalized S1 fEPSP before (a) and after (b) S2 stimulation and individual data points; WT: n = 5/5, APPKI: n = 6/6. p: p value; d: Cohen's effect size. Mean ± S.D. n = n. slices/n. mice. Statistic: generalized linear mixed effect models. Black: WT, green: APPKI.

the probability to generate a population spike during the naturalistic protocol was not different among conditions (Figure 3L, left), differences emerged after separating the stimulation into two frequency bands, non-burst and burst (below and above 50 Hz, respectively). As summarized in Figure 3L (right), the likelihood of generating a population spike was not affected by either genotype or A_1R blocker above 50 Hz (blue area). However, below 50 Hz, the probability of generating a population spike was significantly higher in the APPKI compared to WT. This enhanced probability in APPKI was due to an absence of adenosine-dependent suppression as revealed by the lack of action of the antagonist CPT. These results demonstrated that the TA pathway no longer exhibited high-pass filter properties in response to a naturalistic stimulation in an adenosine-dependent manner.

These results demonstrated an adenosine-dependent increased somatic activity of CA1 neurons in response to signals from both SC and TA terminals and the loss of the homeostatic control in the APPKI model.

Hippocampal adenosine deficiency detected *in vivo* in the APPKI model

The functional data suggested that the adenosine levels might be decreased in the hippocampal brain slices of APPKI mice. To confirm this observation, we employed microdialysis to measure the *in vivo* adenosine levels in the hippocampus.

We implanted a guide canula in WT and APPKI mice at 7 weeks of age; after 1 week of recovery and 12 h before dialysate collection, the probe was implanted targeting CA1 *sr* field (Figure 4A). We collected samples at ZT23-1, at the end of the dark phase when adenosine levels are at their maximum.[43] We found that both absolute levels of adenosine and levels normalized on the percentage of the animal activity were reduced in the APPKI model (Figure 4B). To further confirm that the dialysate reflected physiological levels of adenosine, we collected additional samples from a subset of mice at ZT4-6, a time point when adenosine levels are expected to decrease. Consistent with this expectation, the adenosine concentration decreased at ZT4-6

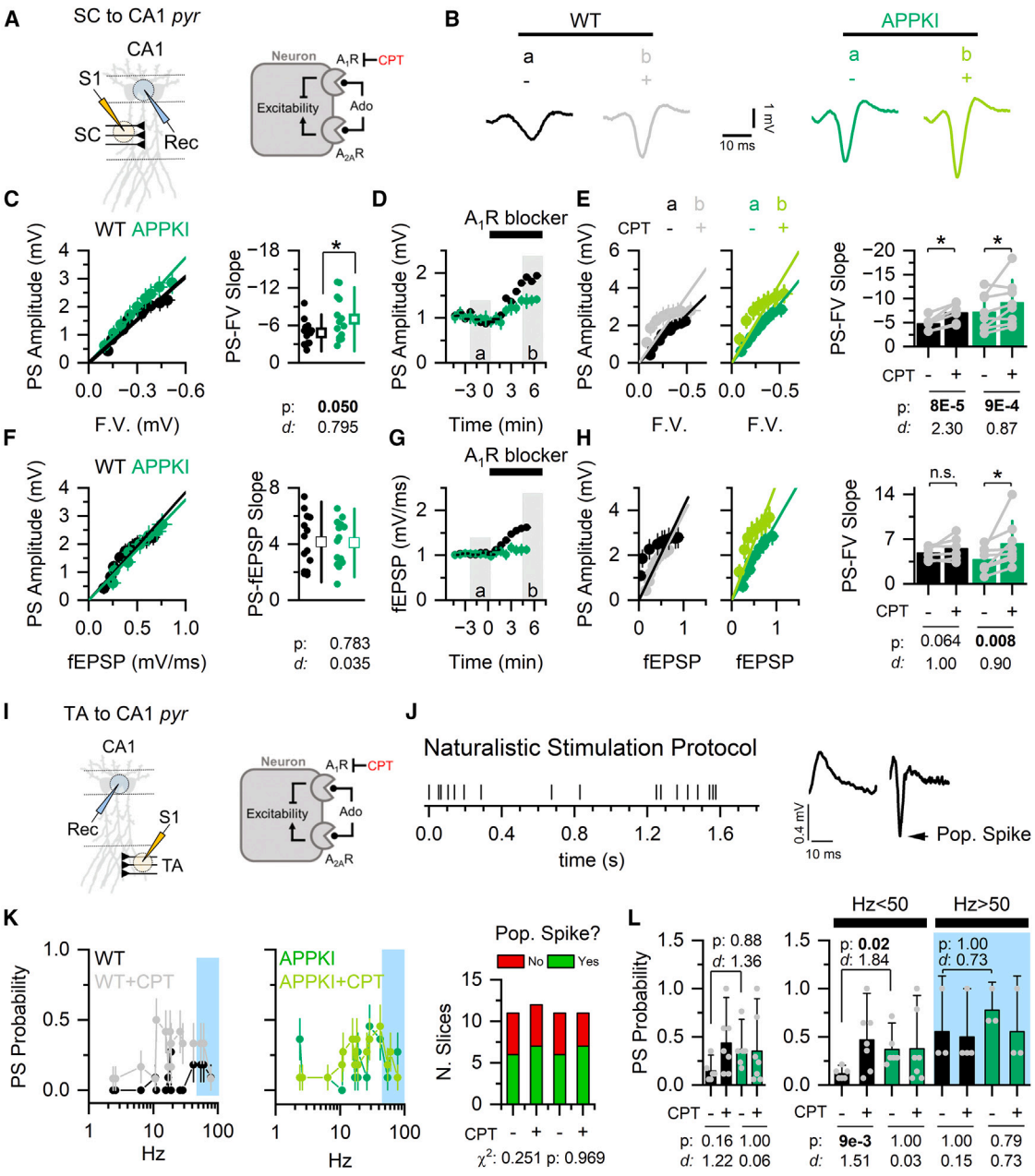

Figure 3. CA1 somatic hyperexcitability reflects synaptic potentiation in the APPKI model

(A and I) Left: scheme of experiment to monitor SC-to-CA1 and TA-to CA1 somatic signaling (S1: stimulation; Rec: recording). Right: cartoon of adenosine signaling.

(B) Representative population spike (PS) traces in the two genotypes before (a) and after (b) the dosage of the A_1R blocker, CPT (200 nM).

(C) Mean PS amplitude-F.V. relationship (left) and individual slope data points (right); WT: n = 15/10; APPKI: n = 14/11.

(D) Time trajectory of PS amplitude before (a) and after (b) dosage of the A_1R blocker.

(E) Mean PS amplitude-F.V. relationship (left) and individual paired slope data points (right) before (a) and after (b) dosage of the A_1R blocker; WT: n = 6/5; APPKI: n = 8/5.

(F) Mean PS amplitude-fEPSP relationship (left) and individual slope data points (right); WT: n = 15/10; APPKI: n = 14/11.

(G) Time trajectory of fEPSP before (a) and after (b) dosage of the A_1R blocker.

(H) Mean PS amplitude-fEPSP relationship (left) and individual paired slope data points (right) before (a) and after (b) dosage of the A_1R blocker; WT: n = 6/5; APPKI: n = 8/5.

(J) Naturalistic stimulation protocol (left) and representative response without and with a population spike evoked (right).

(legend continued on next page)

(Figure 4C), indicating that the adenosine levels were not an artifact caused by tissue damage.

These results supported our indirect adenosine assays that used synaptic and pharmacological approaches and demonstrate that the adenosine levels were reduced *in vivo* in the APPKI model.

CD39/73 ATP-to-adenosine machinery is impaired in the APP KI model

Considering the *in vivo* and *in vitro* evidence of decreased adenosine tone, our objective was to explore the underlying molecular factors contributing to this reduction. We thus analyzed the levels of enzymes involved in the synthesis, degradation, transport, and signaling pathways of adenosine (Figure 4D).

As summarized in Figure 4E, we found that CD39, the rate-limiting enzyme of the two-step extracellular conversion reaction of ATP into adenosine, was significantly downregulated, whereas ADK-L, the nuclear isoform responsible for the adenosine to AMP conversion, was significantly upregulated in the APPKI model. CD73, responsible for the second part of the ATP-to-adenosine reaction, was downregulated, albeit not significantly ($p = 0.055$). Other enzymes involved in the degradation (SAHH, ADA and ADK-S), transport (ENT1), and signaling (A_1R) were not differentially expressed in the two models. We then tested the capacity of the CD39/73 axis to generate adenosine under basal stimulation. We monitored the synaptic response at the SC terminals while simultaneously blocking CD39, CD73, and P2X receptors (to prevent ATP-mediated reduction of synaptic response through P2X receptors), followed by delivery of an ENT1 blocker (to prevent adenosine efflux through the equilibrative transporter after blocking extracellular adenosine production), as summarized in Figure 4G. In the WT model, this cocktail increased net synaptic transmission by reducing ATP-mediated adenosine production. The antagonists were unable to change net synaptic transmission in the APPKI model, demonstrating the inefficiency of the CD39/73 axis to produce basal adenosine from ATP in this genotype (Figures 4H and 4I).

These results demonstrated that the enzymatic machinery (CD39/73 axis) responsible for the extracellular conversion of ATP to adenosine was impaired while ADK-L level was upregulated in the APPKI model.

ADK inhibition normalizes neuronal hyperexcitability in the APPKI model

Given the deficient adenosine tone and increased expression of ADK-L in the APPKI model, we investigated whether the transient administration of 5-iodotubercidin (5-ITU),[44] a non-selective ADK inhibitor, could alleviate the hyperexcitable phenotype and restore the adenosine tone in the APPKI model. This strategy aimed to boost extracellular adenosine levels by inhibiting ADK-S and promote a shift in DNA methylation by inhibiting ADK-L. We administered either the drug (5-ITU) or the vehicle (DMSO) intraperitoneally for 7 days daily starting at 7 weeks of age in the APPKI model. After a week of 5-ITU treatment, there was a significant reduction in both synaptic and somatic activity (Figures 5B–5D). However, the treatment did not restore the adenosine tone synaptically (Figure 5B, left), likely attributed to the washout effect of the drug and its absence during brain slice experiments. In fact, experiments on untreated APPKI brain slices (see Figure S3) perfused acutely with 5-ITU confirmed the ability of 5-ITU to decrease excitability acting through A_1R. Levels of CD73, as opposed to CD39, were increased in response to the *in vivo* administration of 5-ITU (Figure 5E).

These results demonstrated that ADK inhibition during the asymptomatic phase produces long-lasting normalizing effects on neuronal excitability in the APPKI model.

Ketogenic diet normalizes neuronal hyperexcitability and restore adenosine tone in the APPKI model

In addition to its well-recognized recognized positive impact on several AD-related markers,[45,46] the ketogenic diet (KD) has demonstrated its ability to provide anticonvulsant and antiepileptogenic effects by acting through both adenosine-dependent and adenosine-independent pathways.[47] We therefore tested the hypothesis that ketogenic diet could normalize adenosine tone and neuronal hyperexcitability in the APP KI model.

One month of KD regime started at 4 weeks of age (Figure 5F) led to decreased weight (Figure 5G), increased circulating ketone bodies (Figure 5H; normalized on weight), and decreased circulating glucose (Figure 5I; normalized on weight) compared to age-matched mice fed with a regular diet (RD). The KD regime significantly reduced SC to CA1 synaptic hyperexcitability (Figures 5K and 5M) and restored adenosine tone (Figure 5K) in the APPKI model. Similarly, KD reduced the somatic hyperexcitability while leaving intact the somatic adenosine response (Figure 5M). CD73 levels were restored by the KD regime, whereas CD39 levels were only restored in a sex-specific manner (Table S1).

These results demonstrated the efficacy of the ketogenic diet to restore adenosine tone and normalize neuronal excitability in the APPKI model.

DISCUSSION

The present research provides evidence of an association between hippocampal synaptic hyperactivity and adenosine deficiency during the asymptomatic phase in a KI murine model of AD. Reversing aberrant excitatory activity ameliorates the AD trajectory[31]; it is thus relevant to study at which stage and which factors contribute to different forms of neuronal hyperexcitability during the AD trajectory. Here, we focused on the asymptomatic phase (8 weeks) of the disease in an APPKI model aiming to elucidate novel factors contributing to the hippocampal

(K) Mean probability of evoking a population spike (PS Probability) and fraction of slices in which at least 1 PS has been evoked; WT: $n = 6/4$; WT + CPT: $n = 6/4$; APPKI: $n = 6/4$; APPKI+CPT: $n = 7/5$.

(L) PS Probability of slices with at least 1 PS evoked without (left) or with a frequency-band segregation (high frequency: Hz > 50; low frequency: Hz < 50). p: *p* value; *d*: Cohen's effect size. Mean ± S.D. n = n. slices/n. mice. Statistic: generalized linear mixed effect models. Black: WT, green: APPKI, gray: WT + CPT, light green: APPKI+CPT.

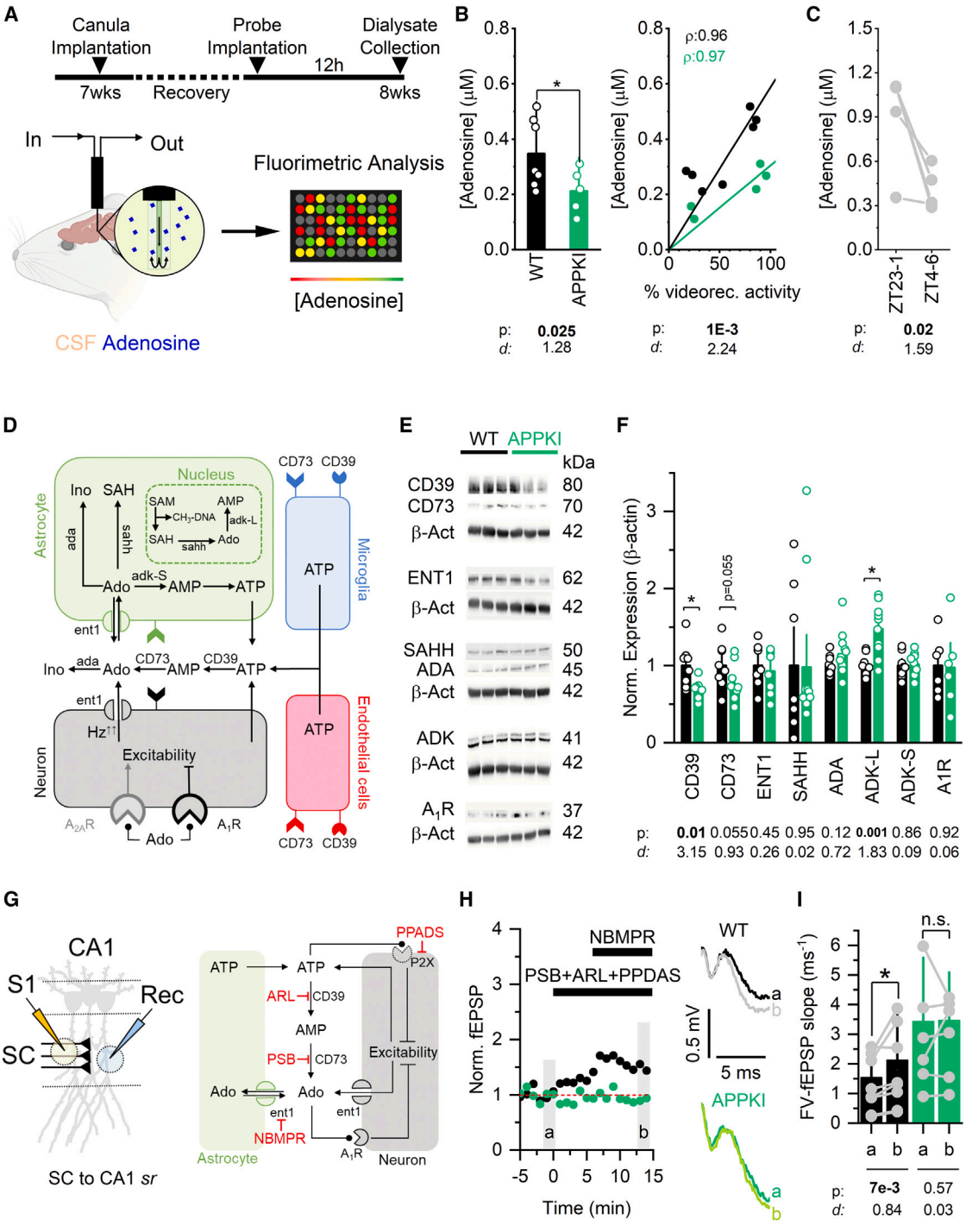

Figure 4. *In vivo* deficiency of adenosine is facilitated by reduced ATP-to-adenosine converting enzymes

(A) Microdialysis and quantification protocol.

(B) Mean adenosine levels (left) and relationship between adenosine concentration and percentage of activity (right) during dialysate collection scored by video monitoring the mice (WT: $n = 7$, APPKI: $n = 5$).

(C) Adenosine levels at ZT33-1 and ZT4-6 (WT: $n = 3$, APPKI: $n = 2$).

(D) Cartoon of the main metabolic reactions and enzymes of adenosine pathway.

(E) Representative western blots and (F) mean normalized expression and single data points. (CD39: WT: $n = 8$, APPKI: $n = 7$; CD73: WT: $n = 8$, APPKI: $n = 7$; ENT1: WT: $n = 7$, APPKI: $n = 8$; SAHH: WT: $n = 8$, APPKI: $n = 11$; ADA: $n = 9$, APPKI: $n = 12$; ADK: WT: $n = 8$, APPKI: $n = 10$; A1R: WT: $n = 6$, APPKI: $n = 6$).

(legend continued on next page)

vulnerability in AD. Considering the disease's progression of the APPKI mouse,[48] the chosen time point precedes the deposition of amyloid plaques at 4 months of age, with prominent deposition of amyloid beta in the medial entorhinal cortex with concomitant impaired gamma phase locking[49] at 5 months of age, progressing with marked amyloid depositions in cortical and hippocampal regions,[50] memory impairment, and astrogliosis at 6 months of age.[48] Although cognitive functions remain intact at 2 months of age, with only minimal grid cell impairment,[51] it is important to emphasize that disease begins decades before symptoms appear in human patients.[1,32] The events occurring during the asymptomatic phase determine the disease's trajectory; accordingly, we focused on this phase to uncover the earliest pathological events and explore the potential for reversing hyperexcitable mechanisms.

In the hippocampus of APPKI mice, we found a potentiated synaptic basal response (SC and TA pathways) in line with previous works.[26] The somatic response scaled with the synaptic activity in both genotypes (Figure 3F), indicating that the enhanced synaptic response in the APPKI spread to the somatic compartment (Figure 3). Accordingly, previous works did not find intrinsic CA1 changes in firing, resting potential, and input resistance.[26] This corroborated the finding that the synapse is an early locus of functional susceptibility. The functional distinction between genotypes became prominent primarily during low-frequency stimulations (Figures 1 and 3), whereas the response to high-frequency stimulations remained largely intact (Figures 2 and 3L), as exemplified by the loss of high-pass filter properties in the TA pathway in APPKI CA1 neurons (Figure 3L). Our findings align with the lack of hippocampal-related behaviors in aged-matched APPKI mice, as hippocampal computations are usually associated with sparse high-frequency neuronal activities. To further support this thesis, we also tested a stimulation protocol that engages both TA and SC terminals and mimics the temporal patterns and rhythmic nature (theta stimulation) of *in vivo* synaptic inputs to CA1 cells as mice traverse their place fields[52] (Figure S4). We monitored two phenomena: phase precession and frequency adaptation. We confirmed that hippocampal theta-phase precession, a behavior involved in spatiotemporal coding and generated within the CA1 field *in vivo*,[53] was observable *in vitro*, and we found that was consistent across genotypes, whereas frequency adaptation appeared to be impaired in the APPKI genotype. This suggests that although the behavioral phenomenon remains intact in the APPKI model, sustaining it might demand higher energy expenditure. In general, even though there are no observable behavioral manifestations at this stage, damage is already occurring at the circuit level. The synaptic hyperactivity reported here and in other studies[26] is suggestive of an increased circuit noise. Under low-intensity and low-frequency presynaptic stimulations, the APPKI CA1 neurons may exhibit a larger and/or more frequent synaptic response compared to WT. This might indicate a compromised ability to filter incoming noisy synaptic communication, while still maintaining intact circuit-level functions associated with high-frequency activities. This increase in system noise level is compatible with the cascading network failure hypothesis,[54] which suggests that even in the absence of observable circuit-level phenotypes, an overloaded system becomes more vulnerable and prone to failure. If noisy signals are not effectively filtered out, this could worsen an ongoing energy crisis that has already been associated with the initial phases of AD development.[55]

Considering the A_1R-mediated inhibitory action of adenosine on hippocampal neuronal activity (presynaptically and postsynaptically),[33] we showed that adenosine levels are reduced *in vivo* (Figures 5B and 5C) and that reduced adenosine tone enables hippocampal hyperexcitability. It is important to note that, although A_1R is also expressed in glial cells[56] and contributions from glia-related mechanisms due to adenosine deficiency cannot be excluded, these factors were not addressed in the present manuscript. However, a recent study demonstrated that astrocytic A_1R deficiency minimally affects neuronal plasticity (LTP).[57] Our findings differed from those seen in later stages of the disease, where inhibiting the activity of adenosine receptors (such as with caffeine) improved synaptic plasticity and behavioral defects.[36] Previous studies showed increased levels of A_1R in advanced disease's stages and different models, including 5XFAD,[58] DeltaK280,[59] 3xTg,[60] and MAPT P301L[60] mice. However, during the asymptomatic stage, we observed intact functional A_1R activation (Figure S2A) and A_1R protein levels (Figure 4E) in the APPKI model. Interestingly, the somatic (Figure 3D), but not the synaptic, A_1R-mediated response was intact, further implying pathology localized at the synaptic level. Aberrant A_{2A}R-mediated signaling contributed to hippocampal deficits in several AD murine models.[61–63] The perfusion of the A_{2A}R blocker in brain slices of the APPKI model (Figure S6) was ineffective in changing the net synaptic transmission, leading us to exclude the involvement of a potentiated A_{2A}R-mediated signaling in the hyperexcitability phenotype.

Despite the TA pathway being unresponsive to the A_1R blocker in both WT and APPKI models while under basal stimulation (0.033Hz), WT, but not APPKI, mice evoked adenosine-dependent responses while applying a naturalistic stimulation (Figure 3O). The synaptic amplitude recorded in the *pyr* layer was significantly larger in the APPKI vs. WT and WT + CPT vs. WT conditions, but not in the APPKI vs. APPKI+CPT comparison (Figure S5), further supporting an impaired capacity to filter incoming low-frequency signals driven by the adenosine deficiency. The absence of a basal A_1R-mediated signaling may be explained by reduced expression of A_1R in the *slm* compared to the *sr* layer of the CA1 field in WT mice.[64,65] Although we do not present a mechanistic explanation, we speculate that the

(G) Left: scheme of experiment to monitor SC-to-CA1 synaptic signaling (S1: stimulation; Rec: recording). Right: cartoon of adenosine signaling and inhibitor targets (cocktail: ARL 67156 trisodium salt: 50 μM; PSB 12379: 50 nM; PPADS tetrasodium salt: 50 μM; NBMPR: 300 nM).
(H) Left: time trajectory of normalized fEPSP before (a) and after (b) the dosage of the drug cocktail. Right: representative traces before (a) and after (b) the dosage of the drug cocktail.
(I) Mean FV-fEPSP slopes before (a) and after (b) drug cocktail and individual data points; WT: n = 8/8, APPKI: n = 6/6.p: p-value; d: Cohen's effect size. Mean ± S.D. n = n. slices/n. mice. Statistic: generalized linear mixed effect models. Black: WT, green: APPKI, gray: WT + cocktail, light green: APPKI+cocktail.

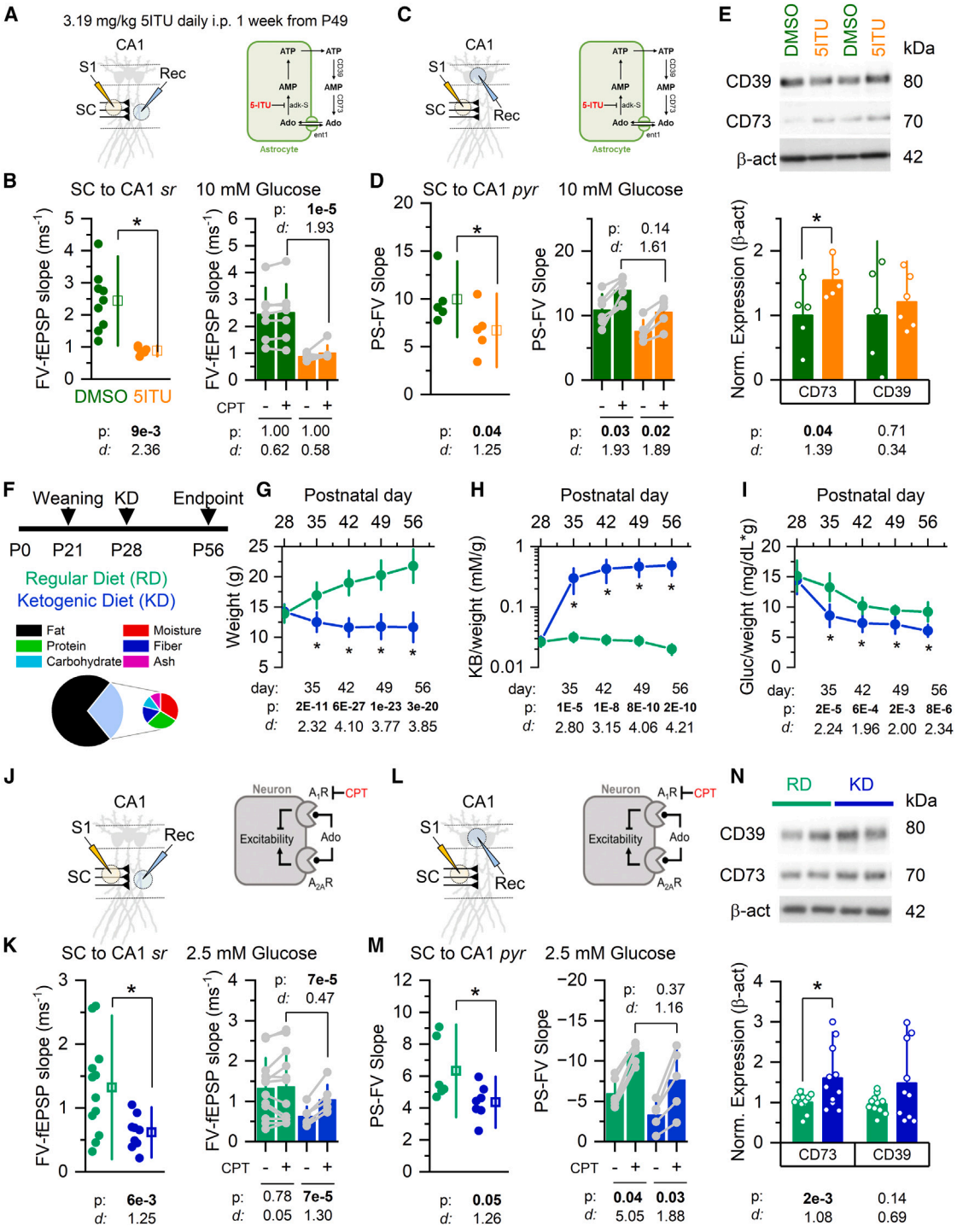

Figure 5. Normalization of neuronal hyperexcitability through pharmacological and ketogenic diet approaches

(A, C, J, and L) Left: scheme of experiment to monitor SC-to-CA1 synaptic and somatic signaling (S1: stimulation; Rec: recording). Right: cartoon of adenosine signaling.

(B) FV-fEPSP data points (left) and individual paired slope data points (right) before (a) and after (b) dosage of the A_1R blocker; DMSO: n = 9/4, 5-ITU: n = 7/6.

(D) PS-FV data points (left) and individual paired slope data points (right) before (a) and after (b) dosage of the A_1R blocker; DMSO: n = 7/4, 5-ITU: n = 7/6.

(E) Top: representative western blots. Bottom: mean normalized expression and single data points (CD73: DMSO: n = 5, 5-ITU:n = 5; CD39: DMSO: n = 5, 5-ITU:n = 6).

(F) Regular diet (RD, green) and ketogenic diet (KD, blue) regime and KD composition. At P28, KD group received *ad libitum* KD for a month (P56). Time trajectories of (G) weight, (H) ketone bodies/weight, and (I) glucose/weight for RD and KD groups.

(legend continued on next page)

adenosine-dependent potentiation of the somatic response could be the result of decreased filtering of the TA signal due a A_1R-mediated change of the axonal resistance in the *sr* field. Alternatively, A_1R-mediated effects may arise from adenosine accumulation in the *slm* layer.

Reduced adenosine tone was driven by reduced levels and activity of CD39/73 enzymes responsible for ATP-to-adenosine conversion, with reports indicating an increase in CD39/73 levels in more advanced stages of the disease.[38] Recent research emphasized the direct role of the microglial CD39/73 axis in facilitating the ATP-to-adenosine conversion and depressing neuronal excitability.[66] Notably, the levels of CD39 appear to positively correlate with the levels of P2Y12R, a homeostatic microglial marker.[67,68] Therefore, it would be important to examine the extent to which microglial activation (and concomitant loss of P2Y12R signature) contributes to the hyperexcitability phenotype observed in APPKI mice. In addition, we found ADK-L, the nuclear isoform of adenosine kinase involved in the DNA methylation process, upregulated in the APPKI model. Of notice, ADK-L is predominantly expressed in astrocytes in the adult mouse,[69] suggesting that hippocampal astrocytes in the APPKI model may exhibit DNA hypermethylation.[70] Although the possibility of neuronal re-expression cannot be ruled out, our findings pave the way for new experimental questions investigating whether astrocytic DNA hypermethylation contributes to neuronal hyperactivity in AD, akin to epilepsy.[70]

The potentiation of adenosine tone has proved advantageous to normalize aberrant neuronal activity.[47] We found that a transient pharmacological restoration of the adenosine tone normalized neuronal excitability, even in the presence of other mechanisms driving the aberrant activity. We pharmacologically inhibited (5-ITU)[44] the activity of ADK (adenosine deaminase kinase), whereas previous manipulations modulated ENT1 activity.[37,38] The administration of the 5-ITU treatment was performed intraperitoneally, making it difficult to rule out potential systemic effects. By selecting an ADK inhibitor, we leveraged adenosine-receptor-dependent and independent effects. In fact, blocking ADK-S (cytosolic isoform) activity rapidly elevates extracellular adenosine levels,[34] whereas blocking ADK-L (nuclear isoform) activity decreases DNA methylation.[44] As the normalization of neuronal activity persisted beyond the duration of the acute drug's effects (Figure S3), this suggested potential epigenetic effects likely involving inhibiting ADK-L and shifting astrocytic DNA methylation state. Further studies are needed to evaluate the functional activity of ADK-L in the context of AD while exploring the astrocytic DNA methylation state. These investigations may reveal adenosine as a crucial link between neuronal activity, metabolic state, and epigenetic modulation.

Given the diverse array of metabolic effects associated with systemically and pharmacologically enhancing adenosine tone, it might not be prudent to employ this strategy as a potential therapeutic intervention in humans. We showed that adenosine levels can be restored and excitability normalized using a non-drug treatment, the ketogenic diet, widening the array of neuroprotective effects of the diet in the AD context. Although the ketogenic diet has been shown to reduce neuroinflammation and plaque deposition in AD preclinical models,[45,71–74] its effectiveness in restoring adenosine tone and normalizing neuronal activity remained unexplored. The normalization of the adenosine tone is likely the results of well-known increase of the ATP levels[45] rather than a restoration of the CD39-73 axis. Since we fed the ketogenic diet to mice between 1 and 2 months of age, it is essential to noticing that this time frame holds developmental significance, and any results obtained may be influenced by concurrent developmental changes.

The results of this study highlighted adenosine signaling as a vulnerability in early AD, and although this might suggest the augmentation of adenosine levels as a viable neuroprotective route of intervention, caution is warranted. Although we found evidence of a neuroprotective role of adenosine augmentation during the asymptomatic stage of AD, other studies observed a beneficial effect by suppressing adenosine receptor signaling in later stages of the disease.[36] Rather than being conflicting, these results indicate that the neuroprotective effects of adenosine augmentation may transition to neurotoxicity depending on the stage of the disease. Moreover, identifying the optimal intervention window for adenosine augmentation currently presents a diagnostic challenge. Further studies are needed to evaluate the long-term effects and identify the optimal time window for the ketogenic diet and ADK inhibition on amyloid beta burden, cognitive function, and overall health. Our results substantiate the need to further explore the causes and consequences of adenosine alterations in the early stages of disease in other murine models and human patients. In fact, comprehending the causes leading to altered adenosine tone (i.e., amyloid-beta-driven cell state transitions, altered metabolism) might illuminate the earliest events of AD. At the same time, investigating both adenosine-receptor-dependent and independent effects (in particular the astrocytic epigenetic effects) on neuronal excitability might provide more targeted strategies of intervention not only for AD but also for other brain disorders. In the present study, we employed a WT murine model as a control of the APPKI. In addition to the familial mutations, the humanized version of the APP sequence (hAPP) further distinguished the two models. To address this, we replicated a subset of functional experiments in the hAPP model (Figure S7), which harbored the humanized APP sequence. The results demonstrated that in the hAPP model the adenosine tone was intact and the excitability physiological, ruling out any contribution of the humanized APP sequence as a driver of the observed differences. In conclusion, we showed that adenosine deficiency compromises synaptic homeostasis contributing to CA1 neuronal hyperexcitability during the presymptomatic stage of an amyloid beta APPKI model.

(K) FV-fEPSP data points (left) and individual paired slope data points (right) before (a) and after (b) dosage of the A_1R blocker; RD: n = 12/12, KD: n = 9/9.
(M) PS-FV data points (left) and individual paired slope data points (right) before (a) and after (b) dosage of the A_1R blocker; RD: n = 6/6, KD: n = 7/7.
(N) Top: representative western blots. Bottom: mean normalized expression and single data points (CD73: RD: n = 11, KD: n = 11; CD39: RD: n = 12, KD: n = 10). p value; d: Cohen's effect size. Mean ± S.D. n = n. slices/n. mice. Statistic: generalized linear mixed effect models. Dark green: APPKI+DMSO, orange: APPKI+5-ITU, light green: APPKI-RD, blue: APPKI-KD.

Limitations of the study

In addition to the previously stated limitations, we used a murine model characterized by aggressive and rapid amyloid beta deposition, with the increase in amyloid beta coinciding with key developmental points. It is thus crucial to assess the generalizability of these results in models with a more physiological evolution of the disease, such as the double KI APP model. Although we focused on the neuronal role of adenosine signaling, it is important to note that adenosine also affects astrocytes, microglia, and endothelial cells. Further studies are needed to elucidate the impact of deficient adenosine tone on cell types beyond neurons.

RESOURCE AVAILABILITY

Lead contact

Further information and requests for resources and reagents should be directed to and will be fulfilled by the lead contact, Philip G. Haydon (philip.haydon@tufts.edu).

Materials availability

This study did not generate new unique reagents.

Data and code availability

- All data points used in the figures formatted in Excel spreadsheet, generated statistical models, and raw western blot images have been deposited at Zenodo: https://zenodo.org/records/13123551 and are publicly available as of the date of publication.
- This paper does not report original code.
- Any additional information required to reanalyze the data reported in this paper is available from the lead contact upon request.

ACKNOWLEDGMENTS

This work was supported by an award from the National Institutes of Health, 5R01AG061838-05 (to G.T. and P.G.H.).

AUTHOR CONTRIBUTIONS

Conceptualization, M.B., A.B., and P.G.H.; methodology, M.B. and A.B.; software, M.B.; investigation, M.B. and A.B.; formal analysis, M.B.; visualization, M.B. and A.B.; data curation, M.B.; writing—original draft, M.B., A.B., and P.G.H.; writing—review & editing, M.B., A.B., T.C.S., T.S., G.T., and P.G.H.; funding acquisition, G.T. and P.G.H.; resources, T.C.S., T.S., and P.G.H.; supervision, M.B. and P.G.H.; project administration, M.B. and P.G.H.

DECLARATION OF INTERESTS

The authors declare no competing interests.

STAR★METHODS

Detailed methods are provided in the online version of this paper and include the following:

SUPPLEMENTAL INFORMATION

Supplemental information can be found online at https://doi.org/10.1016/j.isci.2024.111616.

Received: April 26, 2024
Revised: November 5, 2024
Accepted: November 26, 2024
Published: December 18, 2024

REFERENCES

1. van der Flier, W.M., de Vugt, M.E., Smets, E.M.A., Blom, M., and Teunissen, C.E. (2023). Towards a future where Alzheimer's disease pathology is stopped before the onset of dementia. Nat. Aging *3*, 494–505. https://doi.org/10.1038/s43587-023-00404-2.
2. Palop, J.J., Chin, J., Roberson, E.D., Wang, J., Thwin, M.T., Bien-Ly, N., Yoo, J., Ho, K.O., Yu, G.Q., Kreitzer, A., et al. (2007). Aberrant excitatory neuronal activity and compensatory remodeling of inhibitory hippocampal circuits in mouse models of Alzheimer's disease. Neuron *55*, 697–711. https://doi.org/10.1016/j.neuron.2007.07.025.
3. Vossel, K.A., Beagle, A.J., Rabinovici, G.D., Shu, H., Lee, S.E., Naasan, G., Hegde, M., Cornes, S.B., Henry, M.L., Nelson, A.B., et al. (2013). Seizures and epileptiform activity in the early stages of Alzheimer disease. JAMA Neurol. *70*, 1158–1166. https://doi.org/10.1001/jamaneurol.2013.136.
4. Busche, M.A., and Konnerth, A. (2015). Neuronal hyperactivity–A key defect in Alzheimer's disease? Bioessays *37*, 624–632. https://doi.org/10.1002/bies.201500004.
5. Palop, J.J., and Mucke, L. (2016). Network abnormalities and interneuron dysfunction in Alzheimer disease. Nat. Rev. Neurosci. *17*, 777–792. https://doi.org/10.1038/nrn.2016.141.
6. Zott, B., Busche, M.A., Sperling, R.A., and Konnerth, A. (2018). What Happens with the Circuit in Alzheimer's Disease in Mice and Humans? Annu. Rev. Neurosci. *41*, 277–297. https://doi.org/10.1146/annurev-neuro-080317-061725.
7. Ghatak, S., Dolatabadi, N., Trudler, D., Zhang, X., Wu, Y., Mohata, M., Ambasudhan, R., Talantova, M., and Lipton, S.A. (2019). Mechanisms of hyperexcitability in Alzheimer's disease hiPSC-derived neurons and cerebral organoids vs isogenic controls. Elife *8*, e50333. https://doi.org/10.7554/eLife.50333.
8. Zott, B., Simon, M.M., Hong, W., Unger, F., Chen-Engerer, H.J., Frosch, M.P., Sakmann, B., Walsh, D.M., and Konnerth, A. (2019). A vicious cycle of beta amyloid-dependent neuronal hyperactivation. Science *365*, 559–565. https://doi.org/10.1126/science.aay0198.
9. Babiloni, C., Blinowska, K., Bonanni, L., Cichocki, A., De Haan, W., Del Percio, C., Dubois, B., Escudero, J., Fernández, A., Frisoni, G., et al. (2020). What electrophysiology tells us about Alzheimer's disease: a window into the synchronization and connectivity of brain neurons. Neurobiol. Aging *85*, 58–73. https://doi.org/10.1016/j.neurobiolaging.2019.09.008.
10. Negri, J., Menon, V., and Young-Pearse, T.L. (2020). Assessment of Spontaneous Neuronal Activity In Vitro Using Multi-Well Multi-Electrode Arrays: Implications for Assay Development. eNeuro *7*, ENEURO.0080-19.2019. https://doi.org/10.1523/ENEURO.0080-19.2019.
11. Romoli, M., Sen, A., Parnetti, L., Calabresi, P., and Costa, C. (2021). Amyloid-beta: a potential link between epilepsy and cognitive decline. Nat. Rev. Neurol. *17*, 469–485. https://doi.org/10.1038/s41582-021-00505-9.

12. Lomoio, S., Pandey, R.S., Rouleau, N., Menicacci, B., Kim, W., Cantley, W.L., Haydon, P.G., Bennett, D.A., Young-Pearse, T.L., Carter, G.W., et al. (2023). 3D bioengineered neural tissue generated from patient-derived iPSCs mimics time-dependent phenotypes and transcriptional features of Alzheimer's disease. Mol. Psychiatry *28*, 5390–5401. https://doi.org/10.1038/s41380-023-02147-3.

13. Targa Dias Anastacio, H., Matosin, N., and Ooi, L. (2022). Neuronal hyperexcitability in Alzheimer's disease: what are the drivers behind this aberrant phenotype? Transl. Psychiatry *12*, 257. https://doi.org/10.1038/s41398-022-02024-7.

14. Celone, K.A., Calhoun, V.D., Dickerson, B.C., Atri, A., Chua, E.F., Miller, S.L., DePeau, K., Rentz, D.M., Selkoe, D.J., Blacker, D., et al. (2006). Alterations in memory networks in mild cognitive impairment and Alzheimer's disease: an independent component analysis. J. Neurosci. *26*, 10222–10231. https://doi.org/10.1523/jneurosci.2250-06.2006.

15. Dickerson, B.C., Salat, D.H., Greve, D.N., Chua, E.F., Rand-Giovannetti, E., Rentz, D.M., Bertram, L., Mullin, K., Tanzi, R.E., Blacker, D., et al. (2005). Increased hippocampal activation in mild cognitive impairment compared to normal aging and AD. Neurology *65*, 404–411. https://doi.org/10.1212/01.wnl.0000171450.97464.49.

16. Bookheimer, S.Y., Strojwas, M.H., Cohen, M.S., Saunders, A.M., Pericak-Vance, M.A., Mazziotta, J.C., and Small, G.W. (2000). Patterns of brain activation in people at risk for Alzheimer's disease. N. Engl. J. Med. *343*, 450–456. https://doi.org/10.1056/nejm200008173430701.

17. Amatniek, J.C., Hauser, W.A., DelCastillo-Castaneda, C., Jacobs, D.M., Marder, K., Bell, K., Albert, M., Brandt, J., and Stern, Y. (2006). Incidence and predictors of seizures in patients with Alzheimer's disease. Epilepsia *47*, 867–872. https://doi.org/10.1111/j.1528-1167.2006.00554.x.

18. Mendez, M.F., Catanzaro, P., Doss, R.C., ARguello, R., and Frey, W.H. (1994). Seizures in Alzheimer's disease: clinicopathologic study. J. Geriatr. Psychiatry Neurol. *7*, 230–233. https://doi.org/10.1177/089198879400700407.

19. Vossel, K.A., Ranasinghe, K.G., Beagle, A.J., Mizuiri, D., Honma, S.M., Dowling, A.F., Darwish, S.M., Van Berlo, V., Barnes, D.E., Mantle, M., et al. (2016). Incidence and impact of subclinical epileptiform activity in Alzheimer's disease. Ann. Neurol. *80*, 858–870. https://doi.org/10.1002/ana.24794.

20. Giorgio, J., Adams, J.N., Maass, A., Jagust, W.J., and Breakspear, M. (2024). Amyloid induced hyperexcitability in default mode network drives medial temporal hyperactivity and early tau accumulation. Neuron *112*, 676–686.e4. https://doi.org/10.1016/j.neuron.2023.11.014.

21. Mondragón-Rodríguez, S., Salas-Gallardo, A., González-Pereyra, P., Macías, M., Ordaz, B., Peña-Ortega, F., Aguilar-Vázquez, A., Orta-Salazar, E., Díaz-Cintra, S., Perry, G., and Williams, S. (2018). Phosphorylation of Tau protein correlates with changes in hippocampal theta oscillations and reduces hippocampal excitability in Alzheimer's model. J. Biol. Chem. *293*, 8462–8472. https://doi.org/10.1074/jbc.RA117.001187.

22. Yang, F., Chen, L., Yu, Y., Xu, T., Chen, L., Yang, W., Wu, Q., and Han, Y. (2022). Alzheimer's disease and epilepsy: An increasingly recognized comorbidity. Front. Aging Neurosci. *14*, 940515. https://doi.org/10.3389/fnagi.2022.940515.

23. Kazim, S.F., Seo, J.H., Bianchi, R., Larson, C.S., Sharma, A., Wong, R.K.S., Gorbachev, K.Y., and Pereira, A.C. (2021). Neuronal Network Excitability in Alzheimer's Disease: The Puzzle of Similar versus Divergent Roles of Amyloid β and Tau. eNeuro *8*, ENEURO.0418-20.2020. https://doi.org/10.1523/eneuro.0418-20.2020.

24. Bassett, S.S., Yousem, D.M., Cristinzio, C., Kusevic, I., Yassa, M.A., Caffo, B.S., and Zeger, S.L. (2006). Familial risk for Alzheimer's disease alters fMRI activation patterns. Brain *129*, 1229–1239. https://doi.org/10.1093/brain/awl089.

25. McDonough, I.M., Mayhugh, C., Moore, M.K., Brasfield, M.B., Letang, S.K., Madan, C.R., and Allen, R.S. (2022). Young Adults with a Parent with Dementia Show Early Abnormalities in Brain Activity and Brain Volume in the Hippocampus: A Matched Case-Control Study. Brain Sci. *12*, 496. https://doi.org/10.3390/brainsci12040496.

26. Calafate, S., Özturan, G., Thrupp, N., Vanderlinden, J., Santa-Marinha, L., Morais-Ribeiro, R., Ruggiero, A., Bozic, I., Rusterholz, T., Lorente-Echeverría, B., et al. (2023). Early alterations in the MCH system link aberrant neuronal activity and sleep disturbances in a mouse model of Alzheimer's disease. Nat. Neurosci. *26*, 1021–1031. https://doi.org/10.1038/s41593-023-01325-4.

27. Busche, M.A., Chen, X., Henning, H.A., Reichwald, J., Staufenbiel, M., Sakmann, B., and Konnerth, A. (2012). Critical role of soluble amyloid-β for early hippocampal hyperactivity in a mouse model of Alzheimer's disease. Proc. Natl. Acad. Sci. USA *109*, 8740–8745. https://doi.org/10.1073/pnas.1206171109.

28. Minkeviciene, R., Rheims, S., Dobszay, M.B., Zilberter, M., Hartikainen, J., Fülöp, L., Penke, B., Zilberter, Y., Harkany, T., Pitkänen, A., and Tanila, H. (2009). Amyloid beta-induced neuronal hyperexcitability triggers progressive epilepsy. J. Neurosci. *29*, 3453–3462. https://doi.org/10.1523/jneurosci.5215-08.2009.

29. Bezprozvanny, I., and Mattson, M.P. (2008). Neuronal calcium mishandling and the pathogenesis of Alzheimer's disease. Trends Neurosci. *31*, 454–463. https://doi.org/10.1016/j.tins.2008.06.005.

30. Walton, H.S., and Dodd, P.R. (2007). Glutamate-glutamine cycling in Alzheimer's disease. Neurochem. Int. *50*, 1052–1066. https://doi.org/10.1016/j.neuint.2006.10.007.

31. Gail Canter, R., Huang, W.C., Choi, H., Wang, J., Ashley Watson, L., Yao, C.G., Abdurrob, F., Bousleiman, S.M., Young, J.Z., Bennett, D.A., et al. (2019). 3D mapping reveals network-specific amyloid progression and subcortical susceptibility in mice. Commun. Biol. *2*, 360. https://doi.org/10.1038/s42003-019-0599-8.

32. De Strooper, B., and Karran, E. (2016). The Cellular Phase of Alzheimer's Disease. Cell *164*, 603–615. https://doi.org/10.1016/j.cell.2015.12.056.

33. Cunha, R.A. (2016). How does adenosine control neuronal dysfunction and neurodegeneration? J. Neurochem. *139*, 1019–1055. https://doi.org/10.1111/jnc.13724.

34. Boison, D. (2013). Adenosine kinase: exploitation for therapeutic gain. Pharmacol. Rev. *65*, 906–943. https://doi.org/10.1124/pr.112.006361.

35. Trinh, P.N.H., Baltos, J.A., Hellyer, S.D., May, L.T., and Gregory, K.J. (2022). Adenosine receptor signalling in Alzheimer's disease. Purinergic Signal. *18*, 359–381. https://doi.org/10.1007/s11302-022-09883-1.

36. Cellai, L., Carvalho, K., Faivre, E., Deleau, A., Vieau, D., Buée, L., Blum, D., Mériaux, C., and Gomez-Murcia, V. (2018). The Adenosinergic Signaling: A Complex but Promising Therapeutic Target for Alzheimer's Disease. Front. Neurosci. *12*, 520. https://doi.org/10.3389/fnins.2018.00520.

37. Lee, C.C., Chang, C.P., Lin, C.J., Lai, H.L., Kao, Y.H., Cheng, S.J., Chen, H.M., Liao, Y.P., Faivre, E., Buée, L., et al. (2018). Adenosine Augmentation Evoked by an ENT1 Inhibitor Improves Memory Impairment and Neuronal Plasticity in the APP/PS1 Mouse Model of Alzheimer's Disease. Mol. Neurobiol. *55*, 8936–8952. https://doi.org/10.1007/s12035-018-1030-z.

38. Chang, C.P., Chang, Y.G., Chuang, P.Y., Nguyen, T.N.A., Wu, K.C., Chou, F.Y., Cheng, S.J., Chen, H.M., Jin, L.W., Carvalho, K., et al. (2021). Equilibrative nucleoside transporter 1 inhibition rescues energy dysfunction and pathology in a model of tauopathy. Acta Neuropathol. Commun. *9*, 112. https://doi.org/10.1186/s40478-021-01213-7.

39. Criscuolo, C., Fontebasso, V., Middei, S., Stazi, M., Ammassari-Teule, M., Yan, S.S., and Origlia, N. (2017). Entorhinal Cortex dysfunction can be rescued by inhibition of microglial RAGE in an Alzheimer's disease mouse model. Sci. Rep. *7*, 42370. https://doi.org/10.1038/srep42370.

40. Pascual, O., Casper, K.B., Kubera, C., Zhang, J., Revilla-Sanchez, R., Sul, J.Y., Takano, H., Moss, S.J., McCarthy, K., and Haydon, P.G. (2005). Astrocytic purinergic signaling coordinates synaptic networks. Science *310*, 113–116. https://doi.org/10.1126/science.1116916.

41. Chistiakova, M., Bannon, N.M., Bazhenov, M., and Volgushev, M. (2014). Heterosynaptic plasticity: multiple mechanisms and multiple roles. Neuroscientist *20*, 483–498. https://doi.org/10.1177/1073858414529829.

42. Sun, Q., Buss, E.W., Jiang, Y.Q., Santoro, B., Brann, D.H., Nicholson, D.A., and Siegelbaum, S.A. (2021). Frequency-Dependent Synaptic Dynamics Differentially Tune CA1 and CA2 Pyramidal Neuron Responses to Cortical Input. J. Neurosci. *41*, 8103–8110. https://doi.org/10.1523/JNEUROSCI.0451-20.2021.

43. Halassa, M.M., Florian, C., Fellin, T., Munoz, J.R., Lee, S.Y., Abel, T., Haydon, P.G., and Frank, M.G. (2009). Astrocytic modulation of sleep homeostasis and cognitive consequences of sleep loss. Neuron *61*, 213–219. https://doi.org/10.1016/j.neuron.2008.11.024.

44. Williams-Karnesky, R.L., Sandau, U.S., Lusardi, T.A., Lytle, N.K., Farrell, J.M., Pritchard, E.M., Kaplan, D.L., and Boison, D. (2013). Epigenetic changes induced by adenosine augmentation therapy prevent epileptogenesis. J. Clin. Invest. *123*, 3552–3563. https://doi.org/10.1172/JCI65636.

45. Murano, C., Binda, A., Palestini, P., Baruscotti, M., DiFrancesco, J.C., and Rivolta, I. (2021). Effect of the ketogenic diet in excitable tissues. Am. J. Physiol. Cell Physiol. *320*, C547–C553. https://doi.org/10.1152/ajpcell.00458.2020.

46. Hertz, L., Chen, Y., and Waagepetersen, H.S. (2015). Effects of ketone bodies in Alzheimer's disease in relation to neural hypometabolism, beta-amyloid toxicity, and astrocyte function. J. Neurochem. *134*, 7–20. https://doi.org/10.1111/jnc.13107.

47. Elamin, M., Ruskin, D.N., Sacchetti, P., and Masino, S.A. (2020). A unifying mechanism of ketogenic diet action: The multiple roles of nicotinamide adenine dinucleotide. Epilepsy Res. *167*, 106469. https://doi.org/10.1016/j.eplepsyres.2020.106469.

48. Saito, T., Matsuba, Y., Mihira, N., Takano, J., Nilsson, P., Itohara, S., Iwata, N., and Saido, T.C. (2014). Single App knock-in mouse models of Alzheimer's disease. Nat. Neurosci. *17*, 661–663. https://doi.org/10.1038/nn.3697.

49. Nakazono, T., Jun, H., Blurton-Jones, M., Green, K.N., and Igarashi, K.M. (2018). Gamma oscillations in the entorhinal-hippocampal circuit underlying memory and dementia. Neurosci. Res. *129*, 40–46. https://doi.org/10.1016/j.neures.2018.02.002.

50. Masuda, A., Kobayashi, Y., Kogo, N., Saito, T., Saido, T.C., and Itohara, S. (2016). Cognitive deficits in single App knock-in mouse models. Neurobiol. Learn. Mem. *135*, 73–82. https://doi.org/10.1016/j.nlm.2016.07.001.

51. Jun, H., Bramian, A., Soma, S., Saito, T., Saido, T.C., and Igarashi, K.M. (2020). Disrupted Place Cell Remapping and Impaired Grid Cells in a Knockin Model of Alzheimer's Disease. Neuron *107*, 1095–1112.e6. https://doi.org/10.1016/j.neuron.2020.06.023.

52. Milstein, A.D., Bloss, E.B., Apostolides, P.F., Vaidya, S.P., Dilly, G.A., Zemelman, B.V., and Magee, J.C. (2015). Inhibitory Gating of Input Comparison in the CA1 Microcircuit. Neuron *87*, 1274–1289. https://doi.org/10.1016/j.neuron.2015.08.025.

53. Sloin, H.E., Spivak, L., Levi, A., Gattegno, R., Someck, S., and Stark, E. (2024). Local activation of CA1 pyramidal cells induces theta-phase precession. Science *383*, 551–558. https://doi.org/10.1126/science.adk2456.

54. Jones, D.T., Knopman, D.S., Gunter, J.L., Graff-Radford, J., Vemuri, P., Boeve, B.F., Petersen, R.C., Weiner, M.W., and Jack, C.R., Jr.; Alzheimer's Disease Neuroimaging Initiative (2016). Cascading network failure across the Alzheimer's disease spectrum. Brain *139*, 547–562. https://doi.org/10.1093/brain/awv338.

55. Raut, S., Bhalerao, A., Powers, M., Gonzalez, M., Mancuso, S., and Cucullo, L. (2023). Hypometabolism, Alzheimer's Disease, and Possible Therapeutic Targets: An Overview. Cells *12*, 2019. https://doi.org/10.3390/cells12162019.

56. Boison, D., Chen, J.F., and Fredholm, B.B. (2010). Adenosine signaling and function in glial cells. Cell Death Differ. *17*, 1071–1082. https://doi.org/10.1038/cdd.2009.131.

57. Guo, Q., Gobbo, D., Zhao, N., Zhang, H., Awuku, N.O., Liu, Q., Fang, L.P., Gampfer, T.M., Meyer, M.R., Zhao, R., et al. (2024). Adenosine triggers early astrocyte reactivity that provokes microglial responses and drives the pathogenesis of sepsis-associated encephalopathy in mice. Nat. Commun. *15*, 6340. https://doi.org/10.1038/s41467-024-50466-y.

58. Neuner, S.M., Wilmott, L.A., Hoffmann, B.R., Mozhui, K., and Kaczorowski, C.C. (2017). Hippocampal proteomics defines pathways associated with memory decline and resilience in normal aging and Alzheimer's disease mouse models. Behav. Brain Res. *322*, 288–298. https://doi.org/10.1016/j.bbr.2016.06.002.

59. Dennissen, F.J.A., Anglada-Huguet, M., Sydow, A., Mandelkow, E., and Mandelkow, E.M. (2016). Adenosine A1 receptor antagonist rolofylline alleviates axonopathy caused by human Tau ΔK280. Proc. Natl. Acad. Sci. USA *113*, 11597–11602. https://doi.org/10.1073/pnas.1603119113.

60. Zhou, L.-T., Liu, D., Kang, H.C., Lu, L., Huang, H.Z., Ai, W.Q., Zhou, Y., Deng, M.F., Li, H., Liu, Z.Q., et al. (2023). Tau pathology epigenetically remodels the neuron-glial cross-talk in Alzheimer's disease. Sci. Adv. *9*, eabq7105. https://doi.org/10.1126/sciadv.abq7105.

61. Orr, A.G., Hsiao, E.C., Wang, M.M., Ho, K., Kim, D.H., Wang, X., Guo, W., Kang, J., Yu, G.Q., Adame, A., et al. (2015). Astrocytic adenosine receptor A2A and Gs-coupled signaling regulate memory. Nat. Neurosci. *18*, 423–434. https://doi.org/10.1038/nn.3930.

62. Goncalves, F.Q., Lopes, J.P., Silva, H.B., Lemos, C., Silva, A.C., Gonçalves, N., Tomé, Â.R., Ferreira, S.G., Canas, P.M., Rial, D., et al. (2019). Synaptic and memory dysfunction in a beta-amyloid model of early Alzheimer's disease depends on increased formation of ATP-derived extracellular adenosine. Neurobiol. Dis. *132*, 104570. https://doi.org/10.1016/j.nbd.2019.104570.

63. Lopes, C.R., Silva, A.C., Silva, H.B., Canas, P.M., Agostinho, P., Cunha, R.A., and Lopes, J.P. (2023). Adenosine A2A Receptor Up-Regulation Pre-Dates Deficits of Synaptic Plasticity and of Memory in Mice Exposed to Aβ1–42 to Model Early Alzheimer's Disease. Biomolecules *13*, 1173.

64. Lee, K.S., Schubert, P., Reddington, M., and Kreutzberg, G.W. (1986). The distribution of adenosine A1 receptors and 5'-nucleotidase in the hippocampal formation of several mammalian species. J. Comp. Neurol. *246*, 427–434. https://doi.org/10.1002/cne.902460402.

65. Muñoz, M.-D., and Solís, J.M. (2019). Characterisation of the mechanisms underlying the special sensitivity of the CA2 hippocampal area to adenosine receptor antagonists. Neuropharmacology *144*, 9–18. https://doi.org/10.1016/j.neuropharm.2018.10.017.

66. Badimon, A., Strasburger, H.J., Ayata, P., Chen, X., Nair, A., Ikegami, A., Hwang, P., Chan, A.T., Graves, S.M., Uweru, J.O., et al. (2020). Negative feedback control of neuronal activity by microglia. Nature *586*, 417–423. https://doi.org/10.1038/s41586-020-2777-8.

67. Wang, Y., Cella, M., Mallinson, K., Ulrich, J.D., Young, K.L., Robinette, M.L., Gilfillan, S., Krishnan, G.M., Sudhakar, S., Zinselmeyer, B.H., et al. (2015). TREM2 lipid sensing sustains the microglial response in an Alzheimer's disease model. Cell *160*, 1061–1071. https://doi.org/10.1016/j.cell.2015.01.049.

68. Krasemann, S., Madore, C., Cialic, R., Baufeld, C., Calcagno, N., El Fatimy, R., Beckers, L., O'Loughlin, E., Xu, Y., Fanek, Z., et al. (2017). The TREM2-APOE Pathway Drives the Transcriptional Phenotype of Dysfunctional Microglia in Neurodegenerative Diseases. Immunity *47*, 566–581.e9. https://doi.org/10.1016/j.immuni.2017.08.008.

69. Murugan, M., Fedele, D., Millner, D., Alharfoush, E., Vegunta, G., and Boison, D. (2021). Adenosine kinase: An epigenetic modulator in development and disease. Neurochem. Int. *147*, 105054. https://doi.org/10.1016/j.neuint.2021.105054.

70. Boison, D. (2010). Adenosine dysfunction and adenosine kinase in epileptogenesis. Open Neurosci. J. *4*, 93–101. https://doi.org/10.2174/1874082001004020093.

71. Wu, Y., Gong, Y., Luan, Y., Li, Y., Liu, J., Yue, Z., Yuan, B., Sun, J., Xie, C., Li, L., et al. (2020). BHBA treatment improves cognitive function by targeting pleiotropic mechanisms in transgenic mouse model of Alzheimer's disease. FASEB J. *34*, 1412–1429. https://doi.org/10.1096/fj.201901984R.

72. Shippy, D.C., Wilhelm, C., Viharkumar, P.A., Raife, T.J., and Ulland, T.K. (2020). beta-Hydroxybutyrate inhibits inflammasome activation to attenuate Alzheimer's disease pathology. J. Neuroinflammation *17*, 280. https://doi.org/10.1186/s12974-020-01948-5.

73. Pawlosky, R.J., Kashiwaya, Y., King, M.T., and Veech, R.L. (2020). A Dietary Ketone Ester Normalizes Abnormal Behavior in a Mouse Model of Alzheimer's Disease. Int. J. Mol. Sci. *21*, 1044. https://doi.org/10.3390/ijms21031044.

74. Krishnan, M., Hwang, J.S., Kim, M., Kim, Y.J., Seo, J.H., Jung, J., and Ha, E. (2020). beta-hydroxybutyrate Impedes the Progression of Alzheimer's Disease and Atherosclerosis in ApoE-Deficient Mice. Nutrients *12*, 471. https://doi.org/10.3390/nu12020471.

75. Xiong, G., Metheny, H., Johnson, B.N., and Cohen, A.S. (2017). A Comparison of Different Slicing Planes in Preservation of Major Hippocampal Pathway Fibers in the Mouse. Front. Neuroanat. *11*, 107. https://doi.org/10.3389/fnana.2017.00107.

76. Sadick, J.S., O'Dea, M.R., Hasel, P., Dykstra, T., Faustin, A., and Liddelow, S.A. (2022). Astrocytes and oligodendrocytes undergo subtype-specific transcriptional changes in Alzheimer's disease. Neuron *110*, 1788–1805.e10. https://doi.org/10.1016/j.neuron.2022.03.008.

STAR★METHODS

KEY RESOURCES TABLE

REAGENT or RESOURCE	SOURCE	IDENTIFIER
Antibodies		
Rabbit anti-ADK	Fortis Life Sciences	#A304-280A-T; RRID:AB_2620476
Mouse anti-SAHH	Santa Cruz Biotechnology	#sc-271389; RRID:AB_10612213
Rabbit anti-ADA	AbClonal	#A5151; RRID:AB_2863468
Rabbit anti-CD39	Cell Signaling	#14481; RRID:AB_2798493
Rabbit anti-NT5	Cell Signaling	#13160; RRID:AB_2716625
Rabbit anti-A1R	Proteintech	#55026-1-AP; RRID:AB_10858929
Rabbit anti-ENT1	Proteintech	#11337-1-AP; RRID:AB_2190784
Mouse anti-β-actin	Sigma	#A1978; RRID:AB_476692
HRP-conjugated goat polyclonal anti-rabbit	Thermofisher	#31460; RRID:AB_228341
HRP-conjugated goat polyclonal anti-mouse	Thermofisher	#31430; RRID:AB_228307
Chemicals, peptides, and recombinant proteins		
Sodium chloride	Sigma	S9888
Potassium chloride	Sigma	P3911
Monobasic sodium phosphate	Sigma	S3139
Calcium chloride	Sigma	21115
Magnesium chloride	Sigma	M1028
Glucose	Sigma	G7021
Sucrose	Sigma	S0389
Tris HCl	Sigma	10812846001
Sodium deoxycholate	Sigma	D6750
Triton X-100	Sigma	T8787
SDS	Sigma	L3771
EDTA	Sigma	ED2P
PMSF	Sigma	PMSF-RO
Complete Protease inhibitor cocktail	Millipore Roche	#539131
Halt Phosphatase inhibitor	Themofisher	#1862495
8-cyclopentyl-1,3-dimethylxanthine	Tocris	#6137
2-chloro-N(6)-cyclopentyladenosine	Tocris	#1705
6-S-[(4-Nitrophenyl)methyl]-6-thioinosine	Tocris	#2924
PPADS tetrasodium salt	Tocris	#0625
ARL 67156 trisodium salt	Tocris	#1283
PSB 12379	Tocris	#6083
NuPAGE LDS Sample Buffer	Thermofisher	NP0007
NuPAGE Sample Reducing Agent	Thermofisher	B0009
SDS-PAGE in 4%–12% Bis-Tris gel	Thermofisher	NP0323BOX
NuPAGE™ MOPS SDS Running Buffer	Thermofisher	NP0001
NuPAGE™ Transfer Buffer	Thermofisher	NP0006
Methanol	Sigma	179337
Ponceau Solution	Sigma	P7170
Bovine Serum Albumin	Tocris	#5217
β - Mercaptoethanol		444203
aCSF	Harvard Apparatus	#597316
Critical commercial assays		
Pierce BCA Protein Assay kit	Thermofisher	23225

(*Continued on next page*)

Continued		
REAGENT or RESOURCE	SOURCE	IDENTIFIER
SuperSignal™ West Pico PLUS Chemiluminescent Substrate	Thermofisher	34580
Deposited data	Zenodo	Zenodo: https://zenodo.org/records/13123551
Experimental models: Organisms/strains		
APPNL-G-F/NL-G-F	RIKEN Center for Brain Science	
C57BL/6J mice	The Jackson Laboratory	
hAPP	UCL	
Software and algorithms		
MATLAB		
Origin Lab		
Other		
Guide cannula	Harvard Apparatus	CMAP000137
Microdialysis probe	Harvard Apparatus	CMAP000082
Multi-axis counterbalance arm	Instech	
Two-channel stainless steel swivel	Instech	

EXPERIMENTAL MODEL AND STUDY PARTICIPANT DETAILS

Animal

Homozygous APPKI mice carrying the humanized *App* gene with the Arctic, Swedish and Beyreuther/Iberian mutations ($APP^{NL-G-F/NL-G-F}$[48], C57BL/6J) were supplied by the RIKEN Center for Brain Science. Wild type (WT) C57BL/6J mice were purchased through Jackson Laboratory (Cat# 000664) and used as controls for the APPKI. To control the humanized version of the *App* gene, a subset of experiments has been replicated using homozygous hAPP mice (C57BL/6J) carrying the humanized *App* gene, which were supplied by UCL (Bart De Strooper). To prevent genetic drift due to inbreeding, WT, APPKI, and hAPP mice have been backcrossed with newly purchased WT mice approximately every 10 generations. Adult mice were analyzed between 8 and 9 weeks of age (days: 57.10 ± 2.80; mean ± s.d.). This point corresponded to minimal to no presence of amyloid burden, as well as the absence of tau pathology, gliosis, spine and cellular degeneration, and cognitive impairment in APPKI mice, as previously reported.[26,48] Mice were bred and housed on a 12/12 light/dark cycle. We used the zeitgeber time (ZT) scale that sets the origin of the 24h period (ZT0) to the onset of the light-phase (at ZT12 starts the dark phase), allowing comparison among studies independently of the actual clock-time settings of animal facilities. Mice were fed *ad libitum* with either regular chow (Regular diet; RD) or with Ketogenic diet (KD). KD is formulated as high fat, low carbohydrate diet in a paste form, with the ratio of fat to carbohydrate and protein approximately at 6:1 (F3666, Bio-Serv). KD was administered for a month starting at four weeks of age, with weight, ketone bodies and glucose monitored weekly. For the KD group, heavy loss of weight (more than 50%) and immobility within the first 3 days of the diet were used as exclusion criteria; for the APPKI genotype, about 10% of the mice were excluded within the first week of KD. In all genotypes, both sexes have been used and sex has been included as independent variable in all the analysis. Animals have been single housed only for the microdialysis experiment. For the diet and *in vivo* injection treatments, littermates have been randomly assigned to each group. All animal experiments were approved by The Institutional Animal Care & Use Committee (IACUC) and conducted in accordance with the guideline of the Animal Care and Use Committee of Tufts University.

METHOD DETAILS

Tissue preparation

Hippocampal-entorhinal cortex (HEC) brain slices were prepared from 8 weeks-old male and female mice of the following genotypes: C57BL/6J, hAPP and $hAPP^{NL-G-F/NL-G-F}$ (APP KI[48]). Mice were anesthetized with isoflurane and rapidly decapitated. The brains were removed from the skull and placed in cold modified aCSF cutting solution with 10 mM of glucose (in mM: NaCl 120, KCl 3.2, NaH_2PO_4 1, $CaCl_2$ 1, $MgCl_2$ 2, $NaHCO_3$ 26, Glucose 10) or 2.5 mM glucose (in mM: NaCl 120, KCl 3.2, NaH_2PO_4 1, $CaCl_2$ 1, $MgCl_2$ 2, $NaHCO_3$ 26, Glucose 2.5, Sucrose 7.5). To prepare dorsal hippocampal-entorhinal cortex slices, which guarantees optimal preservation of the perforant path inputs,[75] after removal of the olfactory bulb the brains were glued to an agar ramp (slope 10–12° with the anterior surface facing up the slope) and cut submerged under cold modified aCSF solution into 350 μm thick sections (Leica Vibratome). For electrophysiological experiments with 10 mM glucose, hemislices were then submerged into a storage container filled with aCSF (in mM: NaCl 120, KCl 3.2, NaH_2PO_4 1, $CaCl_2$ 2, $MgCl_2$ 1, $NaHCO_3$ 26, Glucose 10) at 35°C for 30 min and subsequently recovered at room temperature for at least 1 h. For electrophysiological experiments with 2.5 mM glucose, hemislices were submerged into a storage container filled with aCSF (in mM: NaCl 120, KCl 3.2, NaH_2PO_4 1, $CaCl_2$ 2, $MgCl_2$ 1, $NaHCO_3$ 26, Glucose

2.5, Sucrose 7.5) at 35°C for 45 min and subsequently recovered at room temperature for at least 20 min. For western blot tissue preparation, after isolation the slices were moved into a vial containing RIPA (10 mM Tris HCl, 0.1 M, pH 7.2; 1% sodium deoxycholate; 1% Triton X-100; 1% sodium dodecyl sulfate [SDS]; 150 mM NaCl, 1.5 M; 1 mM EDTA, pH 8.0, 0.5 M (#AM9260G, Thermo Fisher Scientific); 1 mM phenylmethanesulfonyl fluoride (#93482, Sigma); Complete Protease Inhibitor cocktail (#539131, Millipore Roche); Halt Phosphatase Inhibitor (#1862495, Thermo Fisher Scientific)). All the solutions were constantly bubbled with 95%–5% O_2-CO_2 mix. All tissue collections have been performed between ZT-23 and ZT-1, a time point at which adenosine concentrations are maximal.

Electrophysiology

Brain hemislices were transferred to a recording chamber mounted on a microscope (Olympus Microscope BX51) and superfused with aCSF saturated with 95%–5% O_2-CO_2. All field potential recordings were performed at 33° ± 1°C with an extracellular glass pipette (7–10 MΩ) filled with aCSF and stimulations were delivered using bipolar tungsten electrodes (FHC #30200). Glutamatergic/GABAergic signals and CA3-to-CA1 connections were left intact in all recordings.

Pharmacology

The A_1R-mediated inhibitory tone was measured by perfusing the slices with the A_1R antagonist 8-cyclopentyl-1,3-dimethylxanthine (CPT, 200 nM; Tocris Bioscience). Sensitivity to A_1R activation was estimated using the A_1R-specific agonist 2-chloro-N(6)-cyclopentyladenosine (CCPA, 10 nM; Tocris Bioscience). Passive production and accumulation of extracellular adenosine was measured indirectly by blocking the equilibrative nucleoside transporter 1 (ENT1) using the transport inhibitor 6-S-[(4-Nitrophenyl) methyl]-6-thioinosine (NBMPR, 100 nM; Tocris Bioscience). PSB 12379 (50 nM; Tocris Bioscience) has been used as CD73 inhibitor. ARL 67156 trisodium salt (50 μM; Tocris Bioscience) has been used to inhibit CD39, since it is a non-selective NTPDase inhibitor. PPADS tetrasodium salt (50 μM; Tocris Bioscience) has been used as non-selective P2 antagonist to prevent the effect of ATP increase in response to the block of the ATP-to-adenosine conversion by PSB+ARL. 5-Iodotubercidin (5-ITU; Tocris Bioscience) has been used as adenosine kinase inhibitor.

Western Blot

Brain slices were prepared as described above. Total protein was extracted by resuspending the isolated tissue in radioimmunoprecipitation assay (RIPA) buffer and stored at −20°C until usage. Samples were then subjected to sonication (Soniprep 150, MSE). The samples were then spun at max vel for 10 min, and supernatants were collected for protein quantification. Protein quantification was performed using a Pierce BCA Protein Assay kit (#23227, Thermo Scientific). 20 μg of total protein were mixed with NuPAGE LDS Sample Buffer (#NP007, Life Technologies), NuPAGE Sample Reducing Agent (#NP0009, Life Technologies), and distilled water prior to being heated at 95°C for 5 min. Proteins were separated by SDS-PAGE in 4%–12% Bis-Tris gel (#NP0336, Thermofisher) using a Novex Bolt Mini Gel system and NuPAGE MOPS SDS Running Buffer (NP0001, Thermofisher) before being transferred onto Immobilon-P polyvinylidene fluoride membranes (#IPVH00010, 0.45 mm pore size; Millipore) in NuPAGE Transfer Buffer with methanol 20% (NP0006, Thermofisher) for 1 h 45 min at 4°C using a Novex Bolt Mini Blot Module. SeeBlue Plus2 standard (#LC5925, Life Technologies) was used to estimate protein sizes, and transfer was confirmed by Ponceau S (#BP103-10, Fisher Biotech) staining. Immunoblot was obtained by first blocking membranes for 1 h at room temperature with a solution of 0.1% Tween 20 and 5% Bovine Serum Albumin (BSA) (#5217, Tocris) in 1× PBS and then incubated with primary antibodies overnight at 4°C (rabbit anti-ADK 1:2000, #A304-280A-T, Fortis Life Sciences; mouse anti-SAHH 1:500, #sc-271389, Santa Cruz Biotechnology; rabbit anti-ADA 1:1000, #A5151, AbClonal; rabbit anti-CD39 1:1000, #14481, Cell Signaling; rabbit anti-NT5 1:1000, #13160, Cell Signaling; rabbit anti-A1R 1:1000, #55026-1-AP, Proteintech; rabbit anti-ENT1 1:500, #11337-1-AP, Proteintech). After washing with 1× PBS Containing 0.1% Tween 20, the membranes were incubated with the species-appropriate horseradish peroxidase-conjugated secondary antibodies (HRP-conjugated goat polyclonal anti-rabbit #31460, Thermofisher; or HRP-conjugated goat polyclonal anti-mouse #31430, Thermo Scientific) for 1 h at room temperature at a 1:20,000 dilution in blocking solution. Immunoreactivity was revealed using SuperSignal West Pico PLUS Chemiluminescent Substrate (#34577, Thermofisher) and imaged using a Fujifilm LAS 4000 Gel Imager system with ImageQuant LAS 4000 software (Fujifilm). If needed, antibodies were stripped from membranes prior to incubation with another primary antibody or prior to incubation with mouse anti- β-actin (1:1000, #A1978, Sigma) in a stripping solution (stripping solution 10%: 7.5% glycine, SDS 1%) with 0.7 β -mercaptoehtanol (#63689, Sigma).

Microdialysis

7 weeks old male and female APPKI or WT mice were anesthetized with isoflurane, injected with buprenorphine (0.5 mg/kg) and placed into a stereotaxic frame. One hole was drilled in the skull (hippocampus coordinates: AP = −2.5, ML = 2 mm) and the guide cannula (#CMAP000137, Harvard Apparatus) was lowered into the hole to reach the coordinate DV = -1.7 mm upon insertion of the microdialysis probe (#CMAP000082, Harvard Apparatus). One anchor screw was inserted in the frontal area to ensure major stability of the system. Anchor screw and guide cannula were then secured to the skull with dental acrylic. 4 days after surgery, mice were moved into an insulated sound-proof chamber and placed into individual Plexiglas circle boxes (Pinnacle Technology, Lawrence, KS) containing water and food *ad libitum*. Mice were left 3 days for habituation prior to data collection and maintained on a 12:12 light/dark cycle. 17-18h before the sample collection at the onset of the light phase (ZT23), the microdialysis probe was inserted into the

guide cannula and connected to a two-channel stainless steel swivel (#375/D/22QM, Instech) attached to a multi-axis counterbalance arm (#MCLA/SMCLA, Instech) to allow free movements of the animal. ACSF (#597316, Harvard Apparatus) was perfused at a rate of 0.2μL/min during the 17-18h prior to sample collection and then switched to 1μL/min at ZT23 and, in a subset of mice, at ZT4. Dialysis samples were stored at −80°C until usage. During sampling, mice were video recorded (Sirenia software, Pinnacle Technology) and subsequently scored as active (mobile or awake) or as inactive (immobile and nested).

Ketone bodies and glucose blood levels

Blood samples were collected weekly to monitor ketone bodies and glucose levels with test strips (Abbott Diabetes Care). Blood was obtained via the tail snip method, which involved applying local disinfectant and anesthesia to the tail, followed by making a 1 mm incision with a scalpel blade, and stopping blood flow by gently dabbing the tail tip. Mice were observed for signs of infection over the subsequent three days.

Intraperitoneal injections

Mice received intraperitoneal (IP) injections of either DMSO or 5-ITU over a 7-day period, starting at 7 weeks of age, administered between ZT-9 and ZT-10. To minimize stress associated with handling, mice were acclimatized to the operator's touch three times a week starting a week before injections. Following the injections, mice were observed for 2 h. Those injected with 5-ITU exhibited reduced mobility, slower heart rate, and shallow breathing for approximately 4 h post-injection. Criteria for exclusion included sustained immobility and weight loss within the initial two days, resulting in the exclusion of about 5% of mice from the 5-ITU group.

QUANTIFICATION AND STATISTICAL ANALYSIS

Electrophysiology

Synaptic basal response

Field excitatory postsynaptic potentials (fEPSP, a proxy of post-synaptic activity) from the CA1b *stratum radiatum* (*sr*) were recorded stimulating the Schaffer collaterals (SC) near the CA1a border at 0.067 Hz (every 15 s). fEPSP from the CA1 *stratum lacunosum moleculare* (*slm*) were recorded stimulating the medial entorhinal cortex layer 3 fibers (temporoammonic pathway; TA) in the CA1 *slm* at 0.067 Hz. Stimulation intensities were delivered in the range 20–100 μA with 10 μA of increment; each stimulation was repeated 4 times and the resulting traces averaged for analysis. Fiber volley (FV, a proxy of pre-synaptic recruitment) amplitude and fEPSP slope (measured in the first 10–30% of the trace after fiber volley to exclude contamination from somatic activation) were used to reconstruct the FV-fEPSP relation and the resulting slope was used as a proxy of net synaptic activity.

Homosynaptic plasticity

fEPSP recordings were taken from the CA1b *sr* by stimulating the Schaffer collaterals near the CA1a border at 0.067 Hz. Stimulation intensities were chosen to produce fEPSP with a slope that was 30–40% of those obtained with maximal stimulation for long-term potentiation (LTP) and paired-pulse ratio (PPr) protocols. The baseline recordings (stimulation at 0.067 Hz) were monitored for 15 min to ensure a stable fEPSP response. LTP was electrically induced at the Schaffer collaterals and recorded at CA1b *sr* by delivering three high-frequency stimulations (HFS, each consisting of 1 s duration 100 Hz train) at 0.033 Hz fEPSPs were measured for 1 h using stimulation of the fibers at 0.067 Hz. The fEPSP slope values were normalized by the average fEPSP values of the pre-stimulation. Analysis was conducted comparing the value of the fEPSP slope pre-stimulation (averaging the last 5 min before HFS) and after 1 h from stimulation (averaging the last 5 min of the hour-long recording post-stimulation). PPr was examined at the CA1 *sr* by stimulating the Schaffer collaterals and monitoring the fEPSP amplitude of two consecutive stimulations with intervals in the range 25–500 ms. After normalizing the fEPSP slopes by the average of the pre-stimulus values, data were expressed as fold change (PPr Ratio) as a function of the interval (ms) between the two consecutive stimulations.

Heterosynaptic plasticity

Heterosynaptic depression recordings were performed by placing two stimulating electrodes in two independent Schaffer collaterals (S1 and S2) and the recording pipette in the CA1b *sr*. Stimulation intensities were chosen to produce fEPSP with a slope that was 20–30% of those obtained with maximal stimulation for both electrodes. Pathway independence was confirmed by monitoring fEPSP amplitude after stimulating the two pathways (S2 preceding S1) at 50 ms interval. Baseline fEPSP slope was monitored for 10–15 min after reaching stable responses by stimulating S1 and S2 pathways (10 s interval) at 0.067 Hz. A 100 Hz 1 s stimulation was then delivered to S2. LTP and heterosynaptic depression were recorded from S2 and S1, respectively, at 0.067 Hz for 10 min. After normalizing the fEPSP slopes by the pre-stimulus values average, the trajectories were reconstructed. Analysis was conducted by averaging the minute before and after the 100 Hz stimulation in both pathways and normalizing the post-stimulation by the pre-stimulation values.

Basal somatic response

Population spikes from the CA1 *stratum pyramidale* (*pyr*) were recorded stimulating the Schaffer collaterals near the CA1a border at 0.067 Hz. Stimulation intensities were delivered in the range 20–100 μA with 10 μA of increment; each stimulation was repeated 4 times and the resulting traces averaged for analysis. FV, fEPSP slope and population spike amplitude (PS, a proxy of somatic activity) were monitored. FV (a proxy of pre-synaptic recruitment) amplitude and PS amplitude were used to reconstruct the FV-PS relation,

and the resulting slope was used as a proxy of net somatic activity. fEPSP slope and PS amplitude were used to reconstruct the fEPSP-PS relation and the resulting slope was used as a proxy of net synaptic transmission to the somatic compartment.

Naturalistic somatic response

fEPSP from the CA1 *pyr* were recorded stimulating the MEC3 fibers (TA pathway) using a naturalistic stimulation protocol (Inter-stimulation interval (s): 0, 0.0532, 0.0661, 0.1046, 0.1394, 0.1927, 0.2862, 0.6734, 0.8293, 1.249, 1.2734,1.3633, 1.4220, 1.4771, 1.5413, 1.5596, 1.5762. Instantaneous frequency (Hz): 18.79, 77.86, 25.95, 28.68, 18.79, 10.69, 2.58, 6.41, 2.38, 41.92, 11.12, 17.03, 18.17, 15.57, 54.50, 60.56) adapted from Sun et al.[42] Stimulation intensities were chosen to produce fEPSP with an amplitude of 0.3–0.35 mV (0.32 ± 0.11 mV). The probability of evoking a population spike (PS Probability) was quantified for each stimulus by visually identifying PS; the average probability of evoking a population spike was computed for each slice and compared among conditions. PS Probability was also plotted based on frequency profile and clustered in burst (Hz > 50) vs. non-burst (Hz < 50) conditions and group comparisons evaluated.

Somatic heterosynaptic response

fEPSP from the CA1 *pyr* were recorded stimulating the TA and Schaffer collateral fibers with a theta protocol adapted from Milstein et al.[52] In detail, five theta cycles (150 ms each), bursts of five stimuli were delivered at 67 Hz (inter-stimulus interval of 15 ms) to both electrodes, with TA stimuli preceding Schaffer collateral stimuli by 20 ms. Stimulation intensities were chosen to produce fEPSP with an amplitude of 0.2–0.25 mV by stimulating the TA terminals and to produce fEPSP without a recognizable PS by stimulating the CA3; on occasions, the minimal stimulation could still elicit a small PS. PS was visually identified; the phase of the first evoked PS in the five theta cycles was evaluated (0.42 ms equivalent to 1°). The frequency of PS was calculated for each cycle and plotted against cycle number. Adaptation index $\frac{1}{N-1}\sum_{n=1}^{N-1}\frac{x_{n+1}-x_n}{x_{n+1}+x_n}$ (where N is the total number of events and x is the chosen parameter) was used to quantify the phase and frequency adaptations over the five theta cycles.

Western Blot

Densitometry measurements were performed using Fiji, with each protein band being normalized to their respective β-actin. For beautification purposes, WB bands in the main figures were cropped. Original blot images are available at https://zenodo.org/records/13123551.

Microdialysis

Adenosine quantification has been conducted using the fluorometric Adenosine Assay Kit (Fluorometric) (Abcam; ab211094). Undiluted microdialysate has been used for the quantification.

Statistic

Statistical analysis has been conducted using generalized linear mixed-effect models (glme) in MATLAB. glme offers a versatile approach for analyzing data deviating from a normal distribution, exhibits heteroskedasticity, and shows dependencies among observations (i.e., nested sampling: multiple brain slices from the same mouse).[76] For each model, the distribution (Normal, Gamma, Inverse Gaussian) and fit method (REMPL, MPL) have been selected by choosing the model maximizing the relative likelihood (i.e., $\mathcal{L}_T = e^{0.5\cdot(AIC_{min}-AIC_i)}$, where AIC_{min} is the minimum AIC across all models and AIC_i is the AIC for the ith model) and visual analysis of the residual. By selecting the model with the largest $\mathcal{L}_T$, we selected the model, among the tested models, that most strongly limits the information loss. For each panel, the number of slices and number of animals are reported in the caption, while p-values and effect sizes (d Coehn's effect size reported as absolute value) are reported in the figure. For independent samples, the effect size has been computed as $d = \frac{\bar{x}_1-\bar{x}_2}{\sqrt{0.5\cdot(s_1^2+s_2^2)}}$, where $\bar{x}_i$ is the average of the ith group and s_i is the standard deviation of the ith group. By using the averaged variance at the denominator, we did not assume homogeneity of variance between groups. Hedge's correction has not been applied. For paired samples, the effect size has been computed as $d = \frac{D}{s_D}$, where D is the averaged difference between paired samples ($D = \frac{\sum_{i=1}^{n}(x_n-y_n)}{n}$, where n is the number of paired measures, x is group 1 and y is group 2) and s_D is the standard deviation of D. For each panel, the dependent and independent variables, and statistical details (F-Statistic, degrees of freedom, p-values) have been summarized in Table S1. For each panel, the model, dataset and modeling parameters are available at https://zenodo.org/records/13123551. Post-hoc analysis has been performed using Bonferroni's correction with alpha = 0.05. No statistical measures were used to estimate sample size, since the effect size was unknown. Experiments were conducted by an investigator with knowledge of animal genotype and treatment. Investigators were blinded during the analysis. Statistical details can be found in each figure, figure legends and Table S1.